Empirically Determined Anisotropic Velocity Distributions and Outflows of O^{5+} Ions in a Coronal Streamer at Solar Minimum

R.A. Frazin[1], S.R. Cranmer, & J.L. Kohl

Harvard-Smithsonian Center for Astrophysics

60 Garden St., Cambridge, MA 02138, USA

ABSTRACT

Empirical constraints on the O^{5+} velocity distributions and outflow speeds in a solar minimum equatorial streamer between 2.6 and 5.1 $R_\odot$ are determined using a spectral synthesis code that includes O VI Doppler dimming. These constraints follow directly from UV spectra taken on 12 October 1996 with the Ultraviolet Coronagraph Spectrometer (UVCS) on the SOHO satellite and 3D electron densities derived from tomography applied to a time series of polarized white-light images taken with the Large Angle and Spectrometric Coronagraph (LASCO) on SOHO. Four conclusions result from this work: 1) our analysis shows O^{5+} velocity distribution anisotropy in the streamer legs and stalk and also shows that the microscopic velocity distribution (which excludes wave motions that equally affect all charged particles) is anisotropic, where the most probable speed perpendicular to the magnetic field direction exceeds that in the parallel direction; 2) there is preferential heating of the O^{5+} ions over the protons in the streamer stalk and legs. 3) There is no evidence for preferential O^{5+} heating in the core; 4) the outflow velocity of the O^{5+} ions is determined at heights above 4.6 $R_\odot$. All results have a confidence level of at least 70%.

1. Introduction

In order to gain insight into the question of how the slow solar wind is heated and accelerated, it is necessary to obtain empirical information about the state of the plasma in the regions where the acceleration and heating take place. The primary source of the slow solar wind at solar minimum is believed to be structures known as coronal streamers, which form at the boundaries of coronal holes (e.g., Feldman et al. 1981, Gosling et al. 1981, however, see Wang 1994 and Wang et al. 1998). Woo (1995) helped to confirm this assertion with a combination of white-light coronagraph observations and speed determinations based on multiple-station interplanetary scintillation measurements. Kohl et al. (1997) used Ultraviolet Coronagraph Spectrometer (UVCS; Kohl et al. 1995) observations of the equatorial streamer seen on 5 February 1997 to estimate O^{5+} outflow

---

[*] also affiliated with the Department of Astronomy, University of Illinois, Urbana, IL 61801, USA

speeds and determine kinetic temperatures for a number of ions. Habbal et al. 1997 used UVCS observations taken in January 1997 to show that stalks (or axes at heights above the cusp) of stable coronal streamers are a source of the slow solar wind. Using the same UVCS data set as Habbal et al., Strachan et al. (2002) made measurements of the O^{5+} outflow speed as a function of latitude. They found the outflow to be less than their sensitivity limit in the center (core) of the streamer. They determined that the outflow speed increases abruptly just outside the streamer legs. Along the streamer stalk, they measured the outflow speed above 3.6 $R_\odot$ and determined that it reaches about 90 km s^{-1} at 5 $R_\odot$. The value of the electron density used by Strachan et al. comes from a Van de Hulst (1950) inversion (which assumes azimuthal symmetry) of polarized white-light data from the Large Angle and Spectrometric Coronagraph (LASCO; Brueckner et al. 1995). Strachan et al. (2000) used tomographic inversion of UVCS O VI data in a Doppler dimming analysis and Van de Hulst inversion of polarized white-light data to determine local O^{5+} outflow speeds and showed that the outflow speeds increase with latitude.

The goal of the work presented here is to use UVCS spectra and a tomographic inversion of LASCO polarized white-light images to constrain kinetic properties (i.e., velocity distribution parameters and outflow speeds) of the O^{5+} ions in a solar-minimum coronal streamer. This analysis also benefits from a new calibration of the overall UVCS pointing (see Frazin 2002).

The O VI λ1031.93, 1037.62 Å doublet (henceforth, separately called λ1032 and λ1037 lines) is useful for constraining kinetic properties because it has large resonantly scattered components. The resonantly scattered component of a coronal spectral line depends on the velocity distribution and outflow speed. We determine constraints on the velocity distributions by comparing the measured O VI (λ1032 to λ1037) intensity ratio to values determined by spectral synthesis. The methods used in this paper are closely related to those described by Cranmer et al. (1999).

2. Observations

2.1. UVCS

The UV data used for this analysis were also presented by Kohl et al. (1997). Spectra containing the O VI λ1032 and λ1037 lines were taken with the UVCS instrument above the west limb at heights ranging from 2.6 to 5.1 $R_\odot$, between 20:10 on 12 October 1996 and 01:00 on 13 October 1996 (UT). The pointing was corrected for both a mirror mechanism non-linearity (see below) and a mirror-grating electronic cross-talk effect (Fineschi, O'Neal & Modigliani 1997). The locations of the UVCS O VI Channel slit are shown superimposed on the LASCO-C2 daily image taken at 23:05 on 12 October 1996 in Figure 1. The nominal heights (marked by the dots in the Figure) are 2.6, 3.1, 3.6, 4.1, 4.6 and 5.1 $R_\odot$. The regions analyzed here are slightly below the dots in the figure.

Except for the data at 2.6 $R_\odot$, the spectra were integrated over 0.312 $R_\odot$, or 303 arcsec, in the

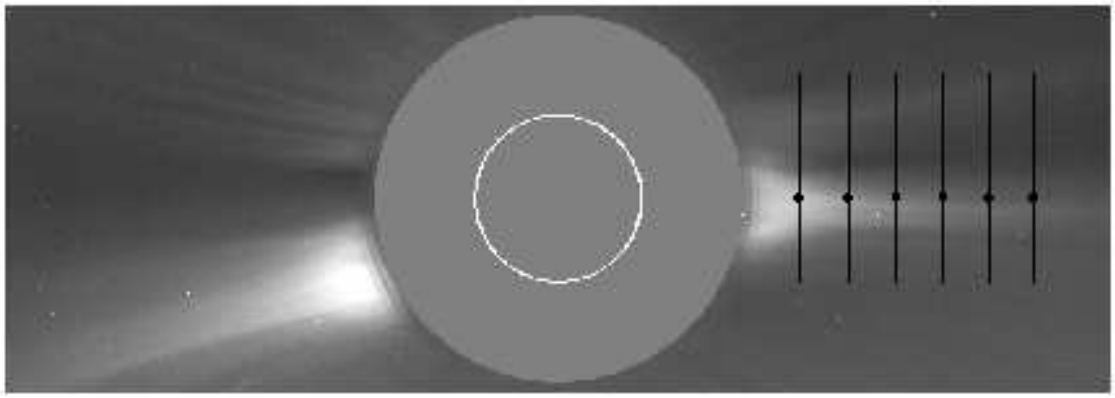

Fig. 1.— The streamer belt at 23:05 UT 12 October 1996 is shown in this LASCO-C2 white-light image of the corona. Superimposed on the image are the UVCS O VI Channel slit fields of view at about 2.6, 3.1, 3.6, 4.1, 4.6 and 5.1 $R_\odot$ (PA = 270° for all). The dots mark the position along the slit that is closest to the limb at each height. The heights refer to the positions of the dots.

north-south direction (along the slit), with the range of integration centered over the maximum of the streamer emission. At 3.1 $R_\odot$ and above, the region of maximum emission was co-spatial in white-light, H I Ly α and the O VI lines. As Figure 2 shows, at 2.6 $R_\odot$, the streamer had a region of depressed O VI emission. Similarly to Raymond et al. (1997), we selected three regions for analysis based on the O VI intensity. Two of the three regions are *legs* (named "LEG1" and "LEG2") and the other is the *core* ("CORE"), with the core containing the central region of depressed O VI emission. The selected spatial extent of both legs was 0.231 $R_\odot$ (224 arcsec) and that of the core was 0.173 $R_\odot$ (168 arcsec) as is shown in Figure 2. We call all of the plasma above 2.6 $R_\odot$ within our 0.312 $R_\odot$ spatial integration region the streamer *stalk*. Our choice of leg and core regions is justified by the fact that the H atoms and O^{5+}ions in LEG1 and LEG2 have similar kinetic properties that are different from those of the region named CORE, as this paper demonstrates.

Figure 3 is an example of an O VI spectrum and the best-fit curve, as determined by the recommended data reduction procedure (DRP; Panasyuk 2002, personal communication). This particular spectrum was taken at 5.1 $R_\odot$. Each spectrum contains 99 bins that cover a wavelength region containing the O VI λ1032, 1037 Å and the H I Ly β λ1025 Å (not shown in Figure 3) lines. We used the DRP to determine the intensities, line widths and uncertainties of the widths of spectral lines used in this analysis. The DRP is a χ^2 curve-fitting procedure described below. No spectral lines other than the three mentioned above were present above the background level, which was determined from the spectral bins that were judged to be unaffected by these three spectral lines (with the assistance of the curve fits made by the DRP). We did not use the DRP to determine the uncertainties in the ratio of the O VI line intensities because the DRP is based on a curve-fitting technique that sometimes produces uncertainty estimates that are as much as a factor of two larger than those derived via a more direct approach, described below. Although the

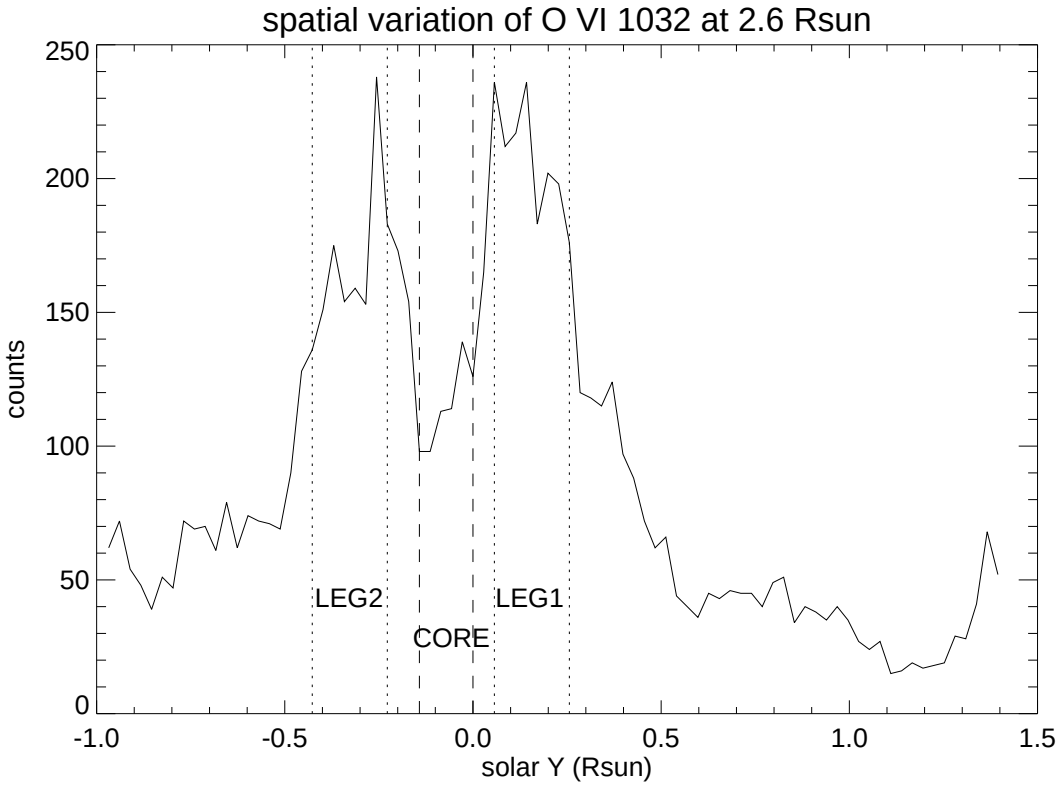

Fig. 2.— The wavelength integrated O VI λ1032 counts at 2.6 $R_\odot$ as a function of position along the slit. The regions labeled "CORE", "LEG1" and "LEG2" were selected for analysis.

two methods sometimes produced different uncertainties, the DRP and the more direct approach produced the same values of the O VI intensity ratio to within less than 1%.

The 1σ radiometric uncertainty of the UVCS instrument is 20% (Gardner et al. 1996; Gardner et al. 2002), however this essentially cancels out in the O VI line ratio. Instead, the uncertainty in the line ratio is dominated by counting statistics and has been estimated as follows:

1. In each spectrum we calculated the mean and variance of the counts in the line-free bins and found that the variance and the mean were nearly equal in most cases, which is consistent with a Poisson distribution. In three cases the background variance was about 50% greater than the mean. We took the background level, i.e. the number of counts per bin not attributable to the spectral lines, to be constant over the spectrum and equal to the mean of the counts in the line-free bins. The square root of the variance of the distribution divided by the square root of the number of background bins was taken to be the uncertainty in the background level. This contribution to the line ratio uncertainty was negligible in every case.

2. We determined the locations of the centers of the O VI lines from the DRP curve fit. We

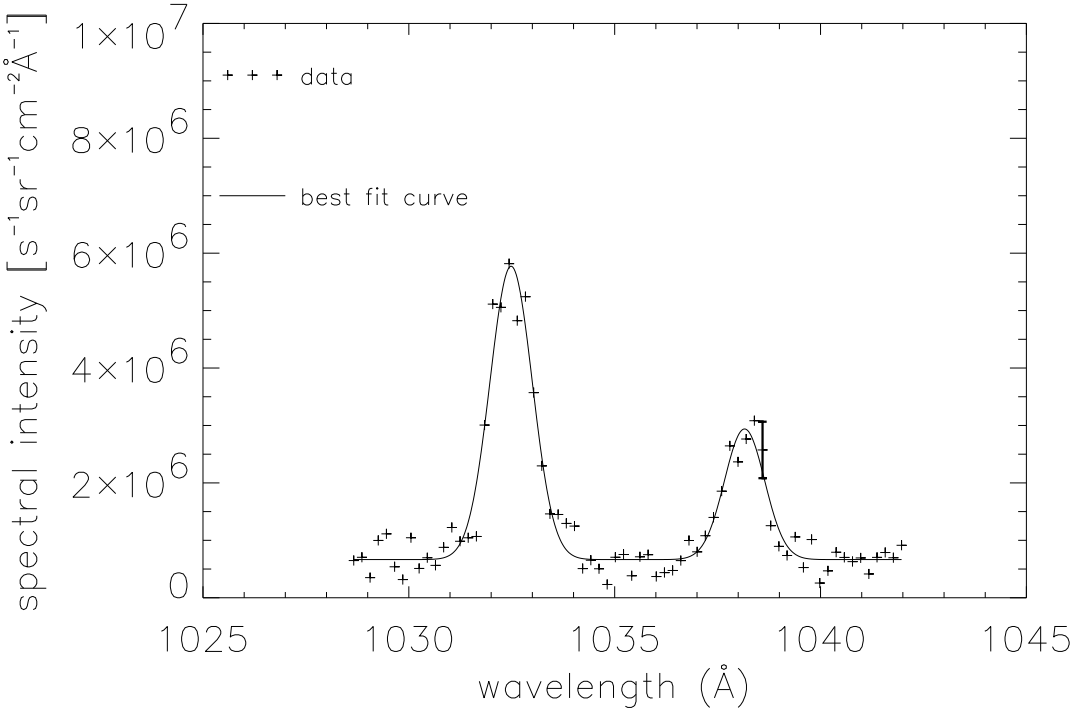

Fig. 3.— Sample O VI λ1032 and λ1037 Å spectrum and best-fit curve. The fitting takes into account the optical characteristics of the UVCS instrument, including stray light. This spectrum was taken at 5.1 $R_\odot$.

chose one region of 5 bins in width, centered over each spectral line. We added the counts in each region and subtracted the background component. We calculated the uncertainty in the ratio of line counts assuming Poisson statistics. We performed the same operation with 7 and 11 bins and found the same result for the line ratio uncertainty. Figure 4 shows how our choices of 5, 7 and 11 bins relate to the line size.

Figures 5 and 6 summarize the results of the curve fits to the UV data. The left panel of Figure 5 shows the intensities of the O VI lines as a function of height. The error bars represent the 20% radiometric uncertainty (the statistical uncertainties are much smaller). The right panel shows the intensity ratio of the O VI λ1032 and λ1037 lines as function of height. Figure 6 is a plot of the $V_{1/e}$ velocities which represent the $1/e$ line widths of the O VI λ1032 and λ1037 spectral lines in the streamer. The widths of the H I Ly α line are also shown for comparison. The Ly α data were taken simultaneously with the O VI data and were integrated over the same spatial regions.

This analysis benefits from the in-flight UVCS pointing calibration (which includes the mirror mechanism non-linearity). The overall position uncertainty is 20 arcsec (Frazin 2002).

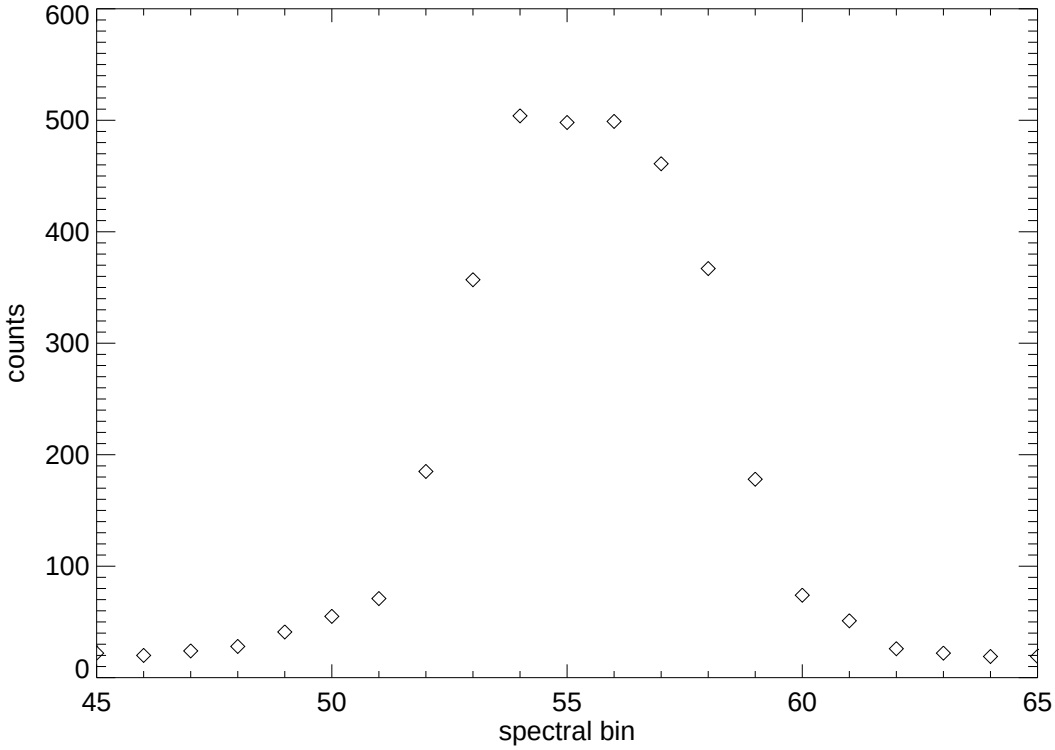

Fig. 4.— A close-up view of O VI λ1032 Å line at 3.1 $R_\odot$. The background level was determined to be 15 counts per bin. The center of the line is in bin 55, and widths of 5, 7, and 11 bins were used to estimate the uncertainty in the O VI line ratio, as described in the text.

On 28 - 31 August 1999 and 2000 the star ρ Leo was within the field of view of UVCS. UVCS was pointed so that the star's light passed through its slits and then UVCS was repointed at a number of positions along the star's trajectory, allowing the star image to drift across the slit in each case. We calculated the star's position relative to the Sun as a function of time and noted times at which the image of the star was in the center (spectral direction) of the UVCS O VI slit. The position of the star at these times yields the pointing calibration information. Frazin (2002) describes this calibration procedure in detail. According to Frazin et al. (2002), a UVCS overall positional uncertainty of 20 arcsec causes less than 10% co-registration uncertainty in the corresponding LASCO pB value. Since the electron density is proportional to the LASCO pB values, the same 10% co-registration uncertainty also applies to the electron density. The spectral diagnostics used in this paper are insensitive to the electron density (see below); therefore this uncertainty has a negligible effect on our results.

Panasyuk (2002, personal communication) fully describes the UVCS data reduction procedure. The DRP is designed to separate coronal line profiles from the light due to other sources and to

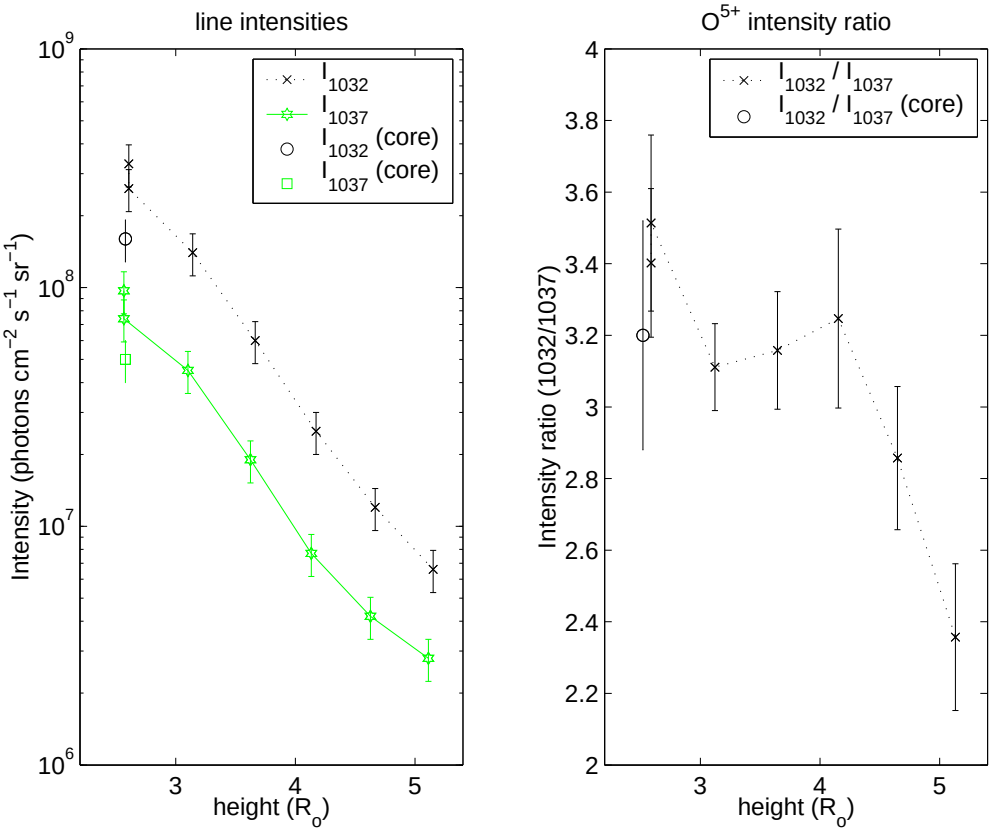

Fig. 5.— Left panel: intensities of the O VI λ1032 and λ1037 lines as a function of height. The error bars are given by the 20% radiometric uncertainty. Right panel: ratio of O VI λ1032 to O VI λ1037 intensity as a function of height. The error bars in the ratio are the result of counting statistics.

compensate for instrumental effects. The DRP fits spectral data obtained from UVCS data files to Gaussian profiles convolved with a trapezoidal profile modeling the spectrometer slit plus, in the case of the Ly α Channel, interplanetary hydrogen and stray light in the instrument. Although there are other options, we used the default settings for the DRP software. With the default settings, the DRP does the following:

1. The data are wavelength calibrated and converted from photon counts to radiometric units. All standard UVCS calibrations are taken into account (Gardner et al. 2002).

2. Distortion resulting in spectral lines being not straight on the detector is corrected.

3. The data are corrected for a detector effect that redistributes the photon counts and creates artificial wings on the profiles. This correction is made with the use of a zero-integral function, as described in Kohl et al. (1997).

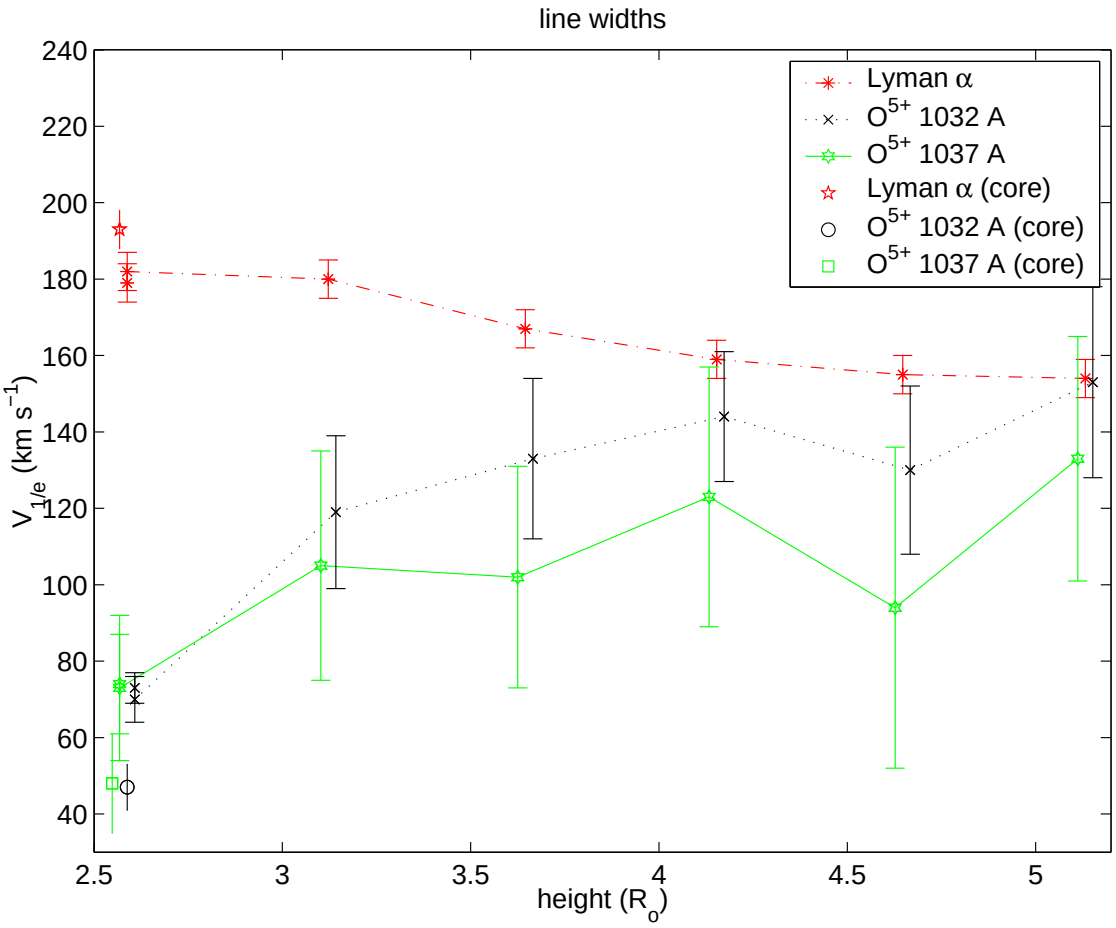

Fig. 6.— Velocities ($V_{1/e}$) corresponding to the line widths of the H I Ly α, O VI λ1032 and λ1037 in the streamer as a function of height. These data were also reported in Kohl et al. (1997).

4. The data are fit to Gaussian profiles convolved with a trapezoidal profile modeling light distribution across the spectrometer slit plus stray light from solar disk emission, and in the case of the Ly α line, interplanetary hydrogen emission. The data are weighted according to Poisson counting statistics. For both the O VI and Ly α channels the (constant) background level is a free parameter and each spectral line is described by three free parameters representing the integral, width and center of a Gaussian. In the case of the Ly α Channel, there are two additional free parameters representing the integral of the stray light (disk) profile and the integral of the interplanetary hydrogen profile. The stray light contribution for the O VI lines is determined from a separate analysis and is not determined via parameter fitting.

5. The standard deviation of the fit parameters and χ^2 value for the fit are calculated based on the assumption of Poisson statistics. The uncertainty in the line width is added in quadrature

to the uncertainty in the intrinsic instrument line width, i.e., the instrument response to a very narrow spectral line (when the slit width is very narrow).

6. The fit parameters are converted to physical units. The line width is corrected for the intrinsic instrument line width and quantization broadening (due to binning of the data and detector pixelation).

2.2. LASCO-C2

We calculated the three dimensional (3D) electron density distribution from white-light polarized brightness (pB) images of LASCO-C2. The images were obtained during the time period 5 through 19 October 1996. LASCO-C2 took one pB image per day, except on 8, 13 and 15 October, for which no C2 pB images are available. The pB images were processed by a program that removes the cosmic ray artifacts and were multiplied by 0.8 to re-normalize them to units of sun-center intensity (pB is usually given either in terms of the solar mean or center intensity. The tomography code requires the sun-center normalization).

Radiometric calibration of LASCO-C2 is described by Howard (2002, *personal communication*). Frazin et al. (2002) show that the LASCO-C2 pB's are generally in agreement with those of the UVCS White Light Channel, whose in-flight calibration is discussed in Romoli et al. (2002).

3. Synthesized line profile computations

We used the most complete description of the relevant plasma emission processes available and we argue that the uncertainties in the calculated values of the O VI intensity ratio are small compared to the uncertainties in the data. The local emissivity of a spectral line depends on the 3D velocity distribution of the ion in question, as is described below. The intensity of an optically thin spectral line l is determined by integrating the emissivity over the line of sight (LOS):

$$I_l(\lambda) = \int_{\rm LOS} \eta_l(\lambda; x) \mathrm{d}x \ , \tag{1}$$

where x is the position along the LOS, λ is the wavelength and $\eta_l(\lambda; x)$ is the emissivity of the relevant spectral line. We define the quantities $I_{1032} \equiv \int_{1032} \int_{\rm LOS} \eta_{1032}(\lambda; x)\, \mathrm{d}x \mathrm{d}\lambda$ and $I_{1037} \equiv \int_{1037} \int_{\rm LOS} \eta_{1037}(\lambda; x)\, \mathrm{d}x \mathrm{d}\lambda$, where the wavelength integrals include only the emission line in question.

The spectral synthesis method used here will be called "the O VI Doppler dimming method" in the rest of this paper. Determining the velocity distribution constraints involves comparing computed values of the ratio of the O VI intensities ($\mathcal{R} \equiv I_{1032}/I_{1037}$) to measured values. The O VI Doppler dimming method has been described by Noci, Kohl, & Withbroe (1987), Li et al. (1998), Noci & Maccari (1999), and references therein. The spectral synthesis code used here is adapted from that used by Cranmer et al. (1999). The spectral synthesis code performs the

computation in equation (1) in two stages. The first stage computes the wavelength-integrated emissivity ($\int \eta_l(\lambda; x)\, \mathrm{d}\lambda$) as a function of x, and the second stage does the integration over x. The first stage requires all of the parameters in table 1 (see below) as inputs, and takes into account all of the relevant geometry and physics of collisional and resonantly scattered emission. Since the electron density N_e is one of the input parameters, the emissivity is automatically correctly weighted by the tomographic value of N_e. Much of the relevant physics is discussed below as we describe the dependence of the emissivity on the parameters in table 1. The spectral synthesis code allows only one of the plasma parameters, N_e, to vary along the LOS. As we will see below, most of the plasma along the LOS is contained within about 20° of the plane of the sky. Since $1/\cos(20°) \approx 1.06$, most of the plasma along a given LOS is nearly equidistant from the Sun and we would expect it to be reasonably homogeneous. Therefore, the plasma properties that we determine in this paper represent a meaningful average over the LOS.

The spectral synthesis code represents the ion velocity distribution as a bi-Maxwellian (see section 3.4). Although this choice is a simplification, it is a useful approximation to any localized (i.e., without separated components such as counter-streaming particles), gyrotropic (again, see section 3.4) velocity distribution, and it allows for anisotropy. Thus, the results given in this paper are approximately correct for any velocity distribution in this class.

The line emissivity η_l depends on the electron density N_e, the electron temperature T_e, the $1/e$ width $w_{||}$ of the velocity distribution parallel to the line from the center of the solar disk to the point of interest in the corona, the $1/e$ width $w_\perp$ of the velocity distribution perpendicular to the line from the center of the solar disk, the outflow speed u, the distance of closest approach of the LOS z, the distance along the LOS x (with $x = 0$ at the point of closest approach), and the deflection angle θ between the flow velocity vector and the line from the center of the solar disk. The parameters $w_{||}$ and $w_\perp$ are the most probable speeds. Table 1 contains a summary of these parameters and how they are determined. The emissivity is also proportional to the chemical abundance, but this parameter cancels out in the O VI intensity ratio and is not included in the table.

symbol	name	source
T_e	electron temperature	electron scattered H I Ly α
N_e	electron density	tomography on LASCO-C2 pB images
$w_{||}$	parallel $1/e$ speed	parameter variation
$w_\perp$	perpendicular $1/e$ speed	measured UV line width
u	parallel outflow speed	parameter variation
z	LOS distance of closest approach	included in LOS integration
x	dist. along LOS	included in LOS integration
θ	deflection angle	set to zero

Table 1: Parameters for determining local emissivity.

3.1. Spatial Parameters

The distance of closest approach z and the distance along the LOS x are specified in the spectral synthesis code during the integration process. The angle of the outflow to the radial direction θ is also required because the Doppler shift of the disk emission that ions see depends on this parameter. We take the outflow to be radial and the radial direction to be the same as the parallel direction. This is equivalent to setting $\theta \equiv 0$. Since the outflow is expected to be close to radial at the heights we study (see the magnetic field model of Banaszkiewicz et al. 1998), this is a good approximation. In support of this conclusion, tomographic reconstructions of the solar minimum corona show that the equatorial streamer structure has little complex structure above 2.5 $R_\odot$. In any case, setting θ to zero picks out the radial component of the outflow speed. Inaccuracies in the value of θ used for the spectral synthesis calculation can be important when the velocity distributions are highly anisotropic and the error in θ is large enough to substantially alter the projection of the velocity distribution onto the plane perpendicular to the radial direction. Futhermore, setting θ to zero is consistent with our goal of setting upper limits on the value of the anisotropy ratio $w_{||}/w_\perp$. Below we show that $w_\perp$ is greater than $w_{||}$. Increasing the value of $\mid \theta \mid$ allows rays from the center of the Sun to "see" the perpendicular part of the velocity distribution, which is broader than the parallel part. This has the effect of lowering the curves in Figures 12 through 16 and can only decrease the values of $w_{||}/w_\perp$ that are consistent with the data. If $w_\perp$ were less than $w_{||}$, increasing $\mid \theta \mid$ would have the opposite effect, but this is only a consideration above 3.6 $R_\odot$, which is well above the cusp of the streamer where the plasma is highly likely to be flowing in the radial direction.

3.2. Electron Temperature

The ratio of the emissivities of the O VI doublet lines is very weakly dependent on T_e because the ionization balance cancels out in the ratio. What little dependence exists is due to the collisional component of the emissivity. Fineschi et al. (1998) used UVCS to make a direct measurement of the electron temperature in a 1996 solar-minimum coronal streamer at 2.7 $R_\odot$ using the Thompson scattered H I Ly α emission from the solar disk. Their measurement yields $T_e = 1.1 \pm 0.3 \times 10^6$ K. We used this electron temperature for all of the calculations in this paper. In an effort to evaluate the effect of uncertainty in T_e, we did calculations with $T_e = 0.5 \times 10^6$ K and $T_e = 2.0 \times 10^6$ K. This changed the synthesized value of $\mathcal{R}$ by only about $\pm 4\%$.

3.3. Electron Density

The intensity ratio $\mathcal{R}$ does not strongly depend on N_e. It depends on N_e to some extent because the two lines have different collisional fractions and the collisional emissivity is proportional to N_e^2 while the resonantly scattered emissivity is proportional to N_e.

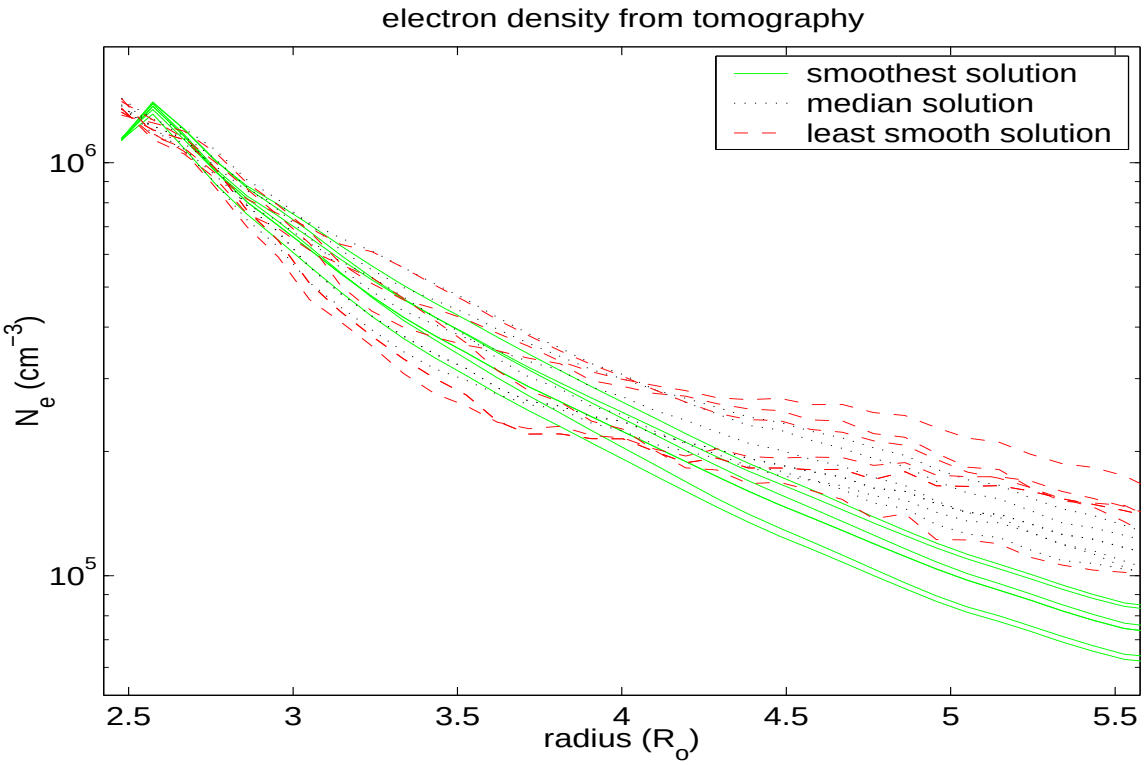

Fig. 7.— Variation of the electron density with radius, as determined by 3D white-light solar rotational tomography. Shown are the most regularized (smoothest), least regularized (least smooth) and median (in between) solutions. The 6 curves for each plotting symbol correspond to axial bins 64 and 65, and angular bins 10, 11 and 12. This plot does not identify the 6 curves from each solution.

The 3D electron density distribution was calculated from LASCO-C2 polarized brightness (pB) images using the Robust, Regularized Positive Estimation (RRPE) method for solar rotational tomography described by Frazin (2000) and Frazin & Janzen (2002). The 3D electron density determination depends on a set of *regularization parameters*. This is a consequence of the fact that the inversion problem is under-determined. A cross-validation analysis shows that the data allow for a range of values of these regularization parameters. Following Frazin & Janzen (2002), we used a cross-validation method to choose three sets of regularization parameters that lead to a most regularized (smoothest), a least regularized (least smooth), and a median (in between) solution.

As with the reconstructions given in Frazin & Janzen (2002), the computation grid is cylindrical, with the axis of the cylinder coincident with the solar rotational pole. It has 64 radial bins, 30 angular (longitudinal) bins, and 130 bins along the cylinder axis (axial bins). This gives an angular grid spacing of 12° and an axial and radial grid spacing of about 0.094 $R_\odot$. At 18:00 UT on 12 October 1996, the Carrington longitude of the SOHO spacecraft was about 38°. The

observations were made above the west limb, which had a Carrington longitude of about 128° at that time, corresponding to angular bin number 11. The solar equatorial plane is located between axial bins 64 and 65. Figure 7 contains 6 curves for each of the three solutions (least, median and most regularized, as mentioned above). The 6 curves show the electron density in axial bins 64 and 65, and in angular bins 10, 11 and 12 as a function of cylindrical radius. The plot distinguishes the three solutions but does not identify the six curves that pertain to each solution.

Figure 8 demonstrates that the Carrington longitude corresponding to the UVCS observations (about 128°, see above) was in the axially symmetric part of the streamer. The figure shows $\sqrt{N_e}$ (in units of $\mathrm{cm}^{-3/2}$) in cylindrical shell cuts at cylindrical radii of 2.6 and 4.1 $\mathrm{R}_\odot$ (median regularized solution). The x-axis is the Carrington longitude, and the y-axis is the height above the equatorial plane, parallel to the axis of the solar pole. This figure shows that the UVCS observations correspond to a part of the coronal structure that was approximately axially symmetric.

The left panel of Figure 9 shows N_e in the vertical slice of the corona corresponding to the plane of the UVCS O VI slit when it was pointed to 4.1 $\mathrm{R}_\odot$. The LOS corresponding to each (spatial) pixel is contained in this plane. The x-axis corresponds to position along the LOS and the y-axis corresponds to the position along the slit. The right panel is the mean of the electron density (as a function of position along the LOS) over the 0.312 $\mathrm{R}_\odot$ region integrated for spectral analysis, as described in section 2.1. All of the results presented here correspond to the median regularization solution.

The ratio $\mathcal{R}$ is insensitive to the choice of the most, median or least regularized solution. In the worst case, 5.1 $\mathrm{R}_\odot$, the choice of tomographic solution causes about $\pm 2\%$ uncertainty in the synthesized value of $\mathcal{R}$. Since the observational uncertainty in the measured value of $\mathcal{R}$ is $\pm 10\%$ at this height, the tomographic contribution to the uncertainty is negligible. Frazin & Janzen (2002) showed that the tomographic solution is not sensitive to the expected levels of statistical noise in the LASCO images, and the effect of such noise on the values of the synthesized O VI line ratio is negligible. Uncertainty in the LASCO-C2 vignetting function below about 2.9 $\mathrm{R}_\odot$ is significant and needs further study (Wang 2002, *personal communication*; Frazin et al. 2002).

3.4. Velocity distribution parameters and Doppler dimming

The object of this paper is to use observations to constrain the velocity distribution parameters $w_\parallel$, $w_\perp$ and u of the O^{5+} ions. These parameters characterize a bi-Maxwellian velocity distribution. A bi-Maxwellian distribution is used because it allows for anisotropy, that is, having different kinetic temperatures parallel and perpendicular to the direction of the magnetic field. Defined in this way, the bi-Maxwellian distribution is *gyrotropic*, meaning that it has rotational symmetry about the magnetic field axis. Although the magnetic field plays no explicit role in this analysis, we take its direction to be radial. This is a good approximation above 2.5 $\mathrm{R}_\odot$ (see section 3.1). The

bi-Maxwellian velocity distribution is given by the function

$$f(v_{\parallel}, v_{\perp}) = \frac{1}{\pi^{3/2} w_{\parallel} {w_{\perp}}^2} \exp\left(-\frac{(v_{\parallel} - u)^2}{{w_{\parallel}}^2} - \frac{v_{\perp}^2}{{w_{\perp}}^2} \right), \quad (2)$$

where $v_{\parallel}$ is a signed scalar representing the velocity in the parallel direction and $v_{\perp}$ is the magnitude of the velocity in the perpendicular direction (e.g., if the z'-axis is along the parallel direction, then $v_{\parallel} = v_{z'}$ and $v_{\perp} \equiv \sqrt{v_{x'}^2 + v_{y'}^2}$).

The resonantly scattered emissivity depends on these parameters because each ion sees a Doppler shifted version of the solar spectrum that depends on its velocity vector (e.g., Noci, Kohl & Withbroe 1987; Li et al. 1998). There are two major effects of interest. First, the mean Doppler shift of the disk light seen by the ions depends primarily on u. The amount of disk light scattered by the ions decreases with increasing u (except in the case of O VI λ1037, in which case an outflow speed in the vicinity of 200 km s^{-1} allows the ions to scatter the disk C II 1036.34, 1037.02 Å emission). Second, the amount of disk light scattered by the ions decreases with increasing $w_{\parallel}$ because as the velocity distribution becomes broader, more of the ions see larger Doppler shifts of the solar disk spectrum (except in the cases when u is large enough to Doppler shift the peak of the distribution away from the disk emission line, so that a large spread in the LOS distribution puts more ions in resonance). These two effects are the basis of the O VI Doppler dimming diagnostic. The dependence of the emissivity on $w_{\perp}$ is small except in situations of extreme anisotropy and would be zero except for the finite angular size of the Sun.

In this paper we use the $V_{1/e}$ corresponding to the measured O VI λ1032 line widths (see Figure 6) as proxies for the most probable speed in the perpendicular direction $w_{\perp}$. This requires justification because the shape of the profile of the emissivity $\eta_l(\lambda)$ depends on all of the parameters in table 1. The line profiles of the scattered components of the λ1032 and λ1037 lines depend on these parameters, due to the complexity of the solar disk's emission line spectrum and the effects of partial frequency redistribution (Mihalas 1978). Because of this complexity, we describe the relationship between the measured values of $V_{1/e}$ and $w_{\perp}$ below.

The only plasma parameter we allow to vary along the LOS in the spectral synthesis process is N_e (see first part of section 3). Even under this restriction, the relationship between the measured $V_{1/e}$ and $w_{\perp}$ is difficult to describe in a few paragraphs. The collisional components and the resonantly scattered components of η_l depend on $w_{\perp}$, $w_{\parallel}$, u and the angle $\omega \equiv \arctan(z/x)$ in different ways. The ratio of collisional to resonantly scattered components depends weakly on T_e (the ionization balance cancels out, but the collisional excitation rate has some dependence) and strongly on N_e (the collisional part is proportion to N_e^2, but the scattered part is proportional to N_e).

In general, determining the relationship between $w_{\perp}$ and the measured $V_{1/e}$ would require complicated iterative analysis (such as performed by Cranmer et al. 1999), but we show that it is not necessary here. Fortunately, when $\omega = 90°$, $V_{1/e}$ of the emissivity, for both the scattered and

collisional components, is nearly equal to $w_\perp$. For the typical values of ω involved in the streamer examined in this paper, the measured value of $V_{1/e}$ differs from $w_\perp$ by less than 20%, as we will see below.

Figure 10 shows N_e as a function of ω for all of the observations, as determined from the tomographic reconstruction. Edge artifacts are quite obvious at above 3.1 $R_\odot$. They are probably due to the fact that emission comes from beyond the confines of the computation cylinder, which has a diameter and height of 12.2 $R_\odot$. The inversion algorithm takes this into account by putting a higher electron density within the cylinder.

As the figure shows, the majority of the electron column is contained within the interval $75^\circ \leq \omega \leq 105^\circ$. In an effort to quantify this further, for each measurement in Figure 6 we calculated the quantity:

$$<\mid \omega - 90^\circ \mid> \equiv \frac{\int_{\rm LOS} N_e(x) \mid \omega(x) - 90^\circ \mid \mathrm{d}x}{\int_{\rm LOS} N_e(x)\, \mathrm{d}x} \,. \tag{3}$$

Table 2 summarizes the results of these calculations. These numbers are underestimates above 3.1 $R_\odot$, for which the LOS cuts a short chord through the computation cylinder. It is not possible to correct for this effect without white-light coronagraph data that extends beyond the field of view of the LASCO-C2 instrument. As Figure 10 shows, below 3.1 $R_\odot$ very little of the electron column is attributed to the edges and the determinations of $<\mid \omega - 90^\circ \mid>$ are not significantly influenced by edge effects.

In an effort to determine an approximate relationship between the measured values of the λ1032 $V_{1/e}$ and $w_\perp$, we evaluated the $1/e$ width of the λ1032 emissivity at each height using $\omega = 90- <\mid \omega - 90^\circ \mid>$, $w_\perp = V_{1/e}$, $N_e \approx N_e(\omega = 70^\circ)$, and for a range of values of the anisotropy ratio $w_\parallel/w_\perp$ and u. We omitted some combinations of parameters not allowed by the analysis presented in section 4.

The results vary little with height and are as follows:

- For $w_\parallel/w_\perp \leq 0.1$ and $u < 50$ km s^{-1}, we have $0.8 < V_{1/e}/w_\perp < 0.9$. For 50 km s^{-1} $< u <$ 150 km s^{-1}, we have $0.95 < V_{1/e}/w_\perp < 1.05$.
- For $0.5 \leq w_\parallel/w_\perp \leq 2.0$ and $u < 150$ km s^{-1}, we have $0.9 < V_{1/e}/w_\perp < 1.1$.
- The anisotropy ratio $w_\parallel/w_\perp = 4.0$ was only evaluated at 5.1 $R_\odot$ for $u = 0$ km s^{-1} and 150 km s^{-1}. In both cases $V_{1/e}/w_\perp \approx 1.24$.

So far we have only considered how the $V_{1/e}$ of the λ1032 emissivity changes with the various parameters. In addition, there is broadening of the observed $V_{1/e}$ due to the fact that the radial outflow vector makes different angles ω with the LOS as a function of position along the LOS x. We show that this effect is negligible for the small values of u we find in this analysis. Because of this effect, a very narrow emissivity would have a measured $V_{1/e}$ of roughly $u \sin(<\mid \omega - 90^\circ \mid>)$.

When the emissivity line width is not negligible, $u \sin(<| \omega - 90^\circ |>)$ is added in quadrature with what the $V_{1/e}$ would be without this effect. In section 4 we will see that for heights of 4.1 $R_\odot$ and less, the maximum allowable value of u is 40 km s^{-1}. The maximum value of $<| \omega - 90^\circ |>$ in table 2 is 24° and $\sin(24^\circ) \approx 0.407$. The smallest measured values of $V_{1/e}$ in Figure 6 are about 50 km s^{-1}. Since $\sqrt{[40 \sin(24^\circ)]^2 + 50^2} \approx 53$, this is less than a 10% effect in the worst case. Above 4.1 $R_\odot$ the maximum allowable value of u is also about equal to the measured value of $V_{1/e}$ and a similar conclusion follows.

4. Empirical O^{5+} velocity distribution and outflow speed constraints

We used the spectral synthesis technique to determine the range of values for $w_\parallel$ and u that fall within the 1σ uncertainty limits of the measured values of $\mathcal{R}$. Although this approach does not, in general, provide enough information to determine individually $w_\parallel$ and u, we were able to determine firm upper limits on the anisotropy ratio $w_\parallel/w_\perp$ and limits on the outflow speed u. The use of line ratios in the O VI Doppler dimming technique greatly reduces the sensitivity to T_e and N_e. We made families of curves and then used the data to determine the parts of the various curves that are observationally allowed. For each measurement of $\mathcal{R}$, we have chosen a number of values of the anisotropy ratio $w_\parallel/w_\perp$, and plotted the calculated value of $\mathcal{R}$ vs. outflow speed u. Only the parts of the curves that fall within (the measured value of) $\mathcal{R} \pm 1\sigma$, where σ is the standard uncertainty in the measured ratio, are considered to be acceptable solutions. In this section we do not reject solutions that may seem physically unrealistic. We leave such judgments to section 5.

Figures 11 through 18 show the calculated $\mathcal{R}$ vs. u curves we used to place constraints on the O^{5+} velocity distributions and outflow speeds. Each value of the anisotropy ratio $w_\parallel/w_\perp$ has a separate curve. In each plot the shaded region is centered on the measured value of $\mathcal{R}$. The width of the shaded region is given by the $\pm 1\sigma$ uncertainty of the measurement. Since we defined this region as the "observationally allowed region," the results given here are 1σ (i.e., $\approx 70\%$ confidence) results. These results are summarized in table 3.

Figure 11 shows the spectral synthesis curves for the streamer core region at 2.6 $R_\odot$. The curves show that the outflow speed is less than about 15 km s^{-1} and that $w_\parallel/w_\perp \leq 1.0$. Since the core is thought to consist of closed-field regions (Raymond et al. 1997), one might expect the velocity distributions to be isotropic. The isotropic solution is consistent with this measured value of $\mathcal{R}$. Figure 12 shows the curves for the streamer LEG1 region at 2.6 $R_\odot$. This figure shows $w_\parallel/w_\perp < 0.5$, and puts an upper limit on the outflow speed of about 10 km s^{-1}. Figure 13 shows the curves for the streamer LEG2 region at 2.6 $R_\odot$. This figure shows $w_\parallel/w_\perp < 0.25$, and puts an upper limit on the outflow speed of about 5 km s^{-1}. It is not likely that the difference in the anisotropy between LEG1 and LEG2 is due to projection effects that mix core and leg material because that would not be consistent with the fact that LEG1 and LEG2 have $\lambda 1032$ $V_{1/e}$ values that are nearly identical (73 ± 5 and 70 ± 5 km s^{-1}, respectively), while the core $V_{1/e}$ is only 47 ± 6 km s^{-1}.

Figure 14 shows the curves for the streamer stalk region at 3.1 $R_\odot$. This figure shows $w_\parallel/w_\perp < 0.6$, and puts an upper limit on the outflow speed of about 30 km s^{-1}. Figure 15 shows the curves for 3.6 $R_\odot$. This figure shows $w_\parallel/w_\perp < 0.7$, and puts an upper limit on the outflow speed of about 40 km s^{-1}. Figure 16 shows the curves for 4.1 $R_\odot$. This figure shows $w_\parallel/w_\perp < 0.6$, and puts an upper limit on the outflow speed of about 35 km s^{-1}.

Figures 17 and 18 pertain to 4.6 and 5.1 $R_\odot$. They show smaller values of $\mathcal{R}$ than at the lower heights and hence allow larger values of u and $w_\parallel/w_\perp$. Figure 17 shows that at 4.6 $R_\odot$, $w_\parallel/w_\perp < 1.6$, and Figure 18 shows that at 5.1 $R_\odot$, $w_\parallel/w_\perp < 4.0$. If $w_\parallel/w_\perp < 0.6$ (see section 5), Figure 17 shows that 40 km $s^{-1} < u < 70$ km s^{-1} at 4.6 $R_\odot$, and Figure 18 shows 50 km $s^{-1} < u < 105$ km s^{-1} at 5.1 $R_\odot$.

5. Discussion

As discussed above, the measured value of $V_{1/e}$ is not a perfect proxy for $w_\perp$ and the constraints on the anisotropy ratios have uncertainties of about 10%.

The higher outflow speeds at 4.6 and 5.1 $R_\odot$ indicated in table 3 require that $w_\parallel/w_\perp < 0.6$ (which is the value of the constraint at 4.1 $R_\odot$). Although it cannot be proved at this time, it seems unlikely that $w_\parallel/w_\perp$ would increase between 4.1 and 5.1 $R_\odot$. Firstly, we know that the O^{5+} ions need to accelerate up to the slow solar wind speed of about 400 km s^{-1} somewhere before 0.3 A.U., and this acceleration is a very plausible explanation of the decrease in the value $\mathcal{R}$ between 4.1 and 5.1 $R_\odot$. Secondly, the value of $w_\perp$ (as determined from the $V_{1/e}$ measurements shown in Figure 6) steadily increases between 3.1 and 5.1 $R_\odot$. Thus, in order for the $w_\parallel/w_\perp > 0.6$ solutions to be valid above 4.1 $R_\odot$, heating in the parallel direction would need to surpass the continued heating in the perpendicular direction. Such behavior would be opposite to that seen at the lower heights. If we are correct in supposing that $w_\parallel/w_\perp < 0.6$ at 4.6 and 5.1, our results show that significant outflow greater than 40 km s^{-1} begins along the streamer axis between about 4.1 and 4.6 $R_\odot$. The constraints on the outflow speeds are not particularly sensitive to the adopted value $w_\parallel/w_\perp$. For example, even a value of $w_\parallel/w_\perp = 1.0$ would not have a large effect on the outflow speed constraint at 5.1 $R_\odot$, as Figure 18 shows.

Comparing the $V_{1/e}$ values in Figure 6 leads to further insights into the kinetic state of the plasma. Except for 2.6 $R_\odot$, the figure shows that the λ1032 $V_{1/e}$ is always greater than that of the λ1037 line, although the differences for the individual data points are within the uncertainties. No known instrumental effects can cause this difference. Furthermore, numerical calculations using the spectral synthesis code always showed the λ1037 line to be broader (usually the difference was quite small) than the λ1032 line over a wide range of parameter space. Several possibilities that might explain this difference come to mind:

- The differences in the $V_{1/e}$ might be explained by the stated uncertainties. This is unlikely,

because (excluding the 2.6 $R_\odot$ points, which are physically different due to the bifurcated streamer structure) there is only a $(0.5)^5$ probability that the λ1032 line always would be broader if the errors are of random sign.

- The line of sight may not be homogeneous in the ion temperature. Since the λ1032 and λ1037 lines have different collisional to scattered fractions, non-homogeneous ion temperatures could theoretically explain the difference, because the collisional emissivity is proportional to N_e^2, while the scattered emissivity is proportional to N_e. Thus, the two lines may be sampling regions of plasma with significantly different kinetic properties.

- The velocity distributions may not be bi-Maxwellian (the velocity distribution may cause the resonantly scattered components of the two lines to have different shapes). Cranmer (2001) and Isenberg et al. (2001) predict non-bi-Maxwellian distributions for O^{5+} ions energized by the damping of ion cyclotron waves.

The measured values of $V_{1/e}$ (which are proxies for $w_\perp$, as explained above) in Figure 6 provide evidence for preferential heating of the O^{5+} ions over the protons (the H velocity distribution is a proxy for that of the protons due to rapid charge transfer between the protons and hydrogen atoms; see Olsen et al. 1994 and Allen et al. 1998) in the legs and stalk of the streamer. The Ly α value decreases from 179 ± 5 km s^{-1} to 154 ± 5 km s^{-1} between 2.6 and 5.1 $R_\odot$, and that of the O VI λ1032 line increases from about 72 ± 5 km s^{-1} (LEG1 and LEG2) to 153 ± 25 km s^{-1}. These values correspond to kinetic temperatures of $(5.0 \pm 0.7) \times 10^6$ K for the O^{5+} and $(1.9 \pm 0.1) \times 10^6$ K for the H at 2.6 $R_\odot$, and $(22.5 \pm 7) \times 10^6$ K for the O^{5+} and $(1.4 \pm 0.1) \times 10^6$ K for the H at 5.1 $R_\odot$.

The spectral lines may be broadened by low-frequency (relative to the ion Larmor frequency) transverse wave motions that impart the same velocity to all species (e.g., Spitzer 1962). The most probable speed $w_\perp$ is the quadrature sum of the microscopic (random) velocity and this wave broadening component. For example, in either leg at 2.6 $R_\odot$, low-frequency motions with a characteristic $1/e$ speed of about 58 km s^{-1} would result in a common perpendicular microscopic temperature of the O^{5+} ions and H atoms of about 1.7×10^6 K. However, at 5.1 $R_\odot$ where the H atoms and O^{5+} ions have the same $1/e$ widths to within the uncertainties, for both species to have the same microscopic temperature would require that nearly all of the observed line width would be due to these transverse motions. Using the values from Figure 6 (154 km s^{-1} for the H, 153 km s^{-1} for the O^{5+}) at 5.1 $R_\odot$ and a characteristic $1/e$ speed of the transverse motions of 152.9 km s^{-1} implies a common microscopic temperature 2.0×10^4 K, which is not a reasonable coronal temperature. It is highly likely that the O^{5+} microscopic temperature is much greater than that of the H when their observed line widths are comparable (above, say, 3 $R_\odot$ for the streamer studied here).

We may use Fe XII λ1242 Å emission (which is seen in the Ly α Channel) to study further the kinetic state of the plasma. The same data set used for all of the other analyses in this paper (i.e., 12 October 1996, above the west limb) contains Fe XII λ1242 Å line profiles. At heights of 2.0, 2.2 and

2.4 $R_\odot$, we spatially integrated the Fe XII emission over the legs of the streamer and found (using the DRP) $V_{1/e}$ values of 47 ± 7, 55 ± 9, and 46 ± 16 km s^{-1}, respectively. Unfortunately, the Fe XII was too weak to be measureable above 2.4 $R_\odot$ in this data set. Since the $V_{1/e}$ values are roughly constant between 2.0 and 2.4 $R_\odot$ to within the uncertainties, it is reasonable to suppose that the $V_{1/e}$ value at 2.6 $R_\odot$ is about 46 km s^{-1} (i.e., the 2.4 $R_\odot$ value). Using this as an upper limit on the broadening due to low-frequency transverse wave motions, we obtain microscopic temperatures of 2.9×10^6 K for the O^{5+}ions and 1.8×10^6 K for the H atoms in the streamer legs at 2.6 $R_\odot$. This suggests that O^{5+} ions are preferentially heated over the protons in the streamer legs. However, adding 14 km s^{-1} (slightly less than the uncertainty) to the Fe XII $V_{1/e}$ value gives an upper limit on the wave broadening of 58 km s^{-1}, and allows for a common microscopic perpendicular temperature of 1.7×10^6 K, as described above.

The Fe XII emission may also be used to help elucidate the nature of the O^{5+} anisotropy. Again, using the Fe XII line width as an upper limit on the low-frequency transverse wave motions, we show that the O^{5+} microscopic velocity distribution (excluding bulk fluid motions) is anisotropic in the streamer legs. In LEG1, where $w_\parallel / w_\perp < 0.5$, the upper limit on $w_\parallel$ is about 0.5×73 km s^{-1}, or 37 km s^{-1}. Subtracting a wave broadening component 46 km s^{-1} in quadrature gives $w_\perp{}' = 57$ km s^{-1} ($w_\perp{}'$ is the microscopic most probable speed in the perpendicular direction), which is greater than $w_\parallel$ and therefore corresponds to a microscopically anisotropic distribution. However, adding 16 km s^{-1} (the uncertainty in the Fe XII line width) and thus taking the wave broadening to be 62 km s^{-1}, gives $w_\perp{}' = 39$ km s^{-1}, which essentially corresponds to a microscopically isotropic distribution. In LEG2, where $w_\parallel / w_\perp < 0.25$ and $w_\perp \approx 70$ km s^{-1}, $w_\parallel$ is 17 km s^{-1}. Again, using 46 and 62 km s^{-1} for the broadening gives $w_\perp{}'$ values of 53 and 39 km s^{-1}, respectively, indicating strong microscopic anisotropy in both cases. Thus, we conclude that our measurements show the O^{5+} velocity distributions to be microscopically anisotropic in both streamer legs at 2.6 $R_\odot$. This result has a confidence level of at least 70%. The fact that the Fe XII line width is an upper limit on the low-frequency wave broadening component serves to increase the confidence in this result.

In contrast to the streamer legs and stalk, the values of $V_{1/e}$ in the streamer core are consistent with proton and O^{5+} thermodynamic equilibrium to within the uncertainties. The Ly α value is 193 ± 5 km s^{-1} and corresponds to a kinetic temperature of $(2.2 \pm 0.1) \times 10^6$ K, and the λ1032 line width is 47 ± 6 km s^{-1} and corresponds to kinetic temperature of $(2.1 \pm 0.5) \times 10^6$ K.

It is thought that the streamer core consists of magnetic loops anchored in the photosphere and that it does not participate in a major way in the slow solar wind (although Wang et al. 1998 and Wu et al. 2000 suggest these loops at times may reconnect with the open fields and cause transient effects in the flow) and that the legs consist of open field lines and participate in the primary flow. The UVCS observations and analysis of Raymond et al. (1997), show that the elemental abundances in the legs closely correspond to those measured *in-situ* in the slow solar wind, while the elemental abundances in the core do not. The above kinetic analysis allows for additional differences between the legs and core. Table 3 shows that while LEG2 and the CORE have substantially different upper limits on $w_\parallel / w_\perp$, LEG1 is in between.

As a side note, we mention that the study of a mid-latitude streamer in the ascending phase of the solar cycle conducted by Frazin et al. (1999) shows that the width of the O VI λ1032 line has a far less dramatic increase with height, with $V_{1/e}$ increasing from 59 km s^{-1} at 1.6 R$_\odot$ to only 78 km s^{-1} at 5.4 R$_\odot$.

The evidence for microscopic anisotropy in the O^{5+} velocity distributions and preferential heating of the O^{5+} ions over the protons presented here is reminiscent of that provided for coronal holes by Cranmer et al. (1999). One particularly favorable candidate mechanism to explain these phenomena is *ion cyclotron resonance*, in which high-frequency Alfvén waves are absorbed by the heavy ions. Cranmer et al. discuss the relevance of this process to an empirical model of a polar coronal hole. Our data suggest that the dominant processes that heat the heavy ions in coronal holes may also be important in streamers.

Although the widths of the O VI λ1032 and λ1037 lines are not found to be exactly the same, they only differ by a small amount. This near agreement lends credence to the practice adopted here of treating the spectroscopic quantities as indicative of average plasma quantities along the LOS. The line intensity ratio $\mathcal{R}$ is mostly affected by the outflow speed u and parallel most probable speed $w_{||}$, and differences between the line widths are mostly affected by correlations along the LOS between the perpendicular most probable speed $w_\perp$ and the electron density N_e. Since the line widths are nearly the same, it is highly likely that correlations between $w_\perp$ and N_e are insignificant (coronal hole observations over the solar cycle indicate a strong correlation between these two parameters [Miralles et al. 2001, 2001b]) and that these quantities do not fluctuate far from their means. Furthermore, it is unlikely to have a situation in which $w_\perp$ and N_e do not significantly vary along the LOS while $w_{||}$ and u vary considerably. We have also shown that results of this work are insensitive to N_e and T_e. We therefore conclude that even though we have represented the plasma along the LOS as homogeneous, this choice is unlikely to significantly affect the primary conclusions of this work. We are left with results that are constrained by the 1σ error bars of the various measurements. As discussed above, the determination of the outflow speed at 5.1 R$_\odot$ depends on the anisotropy of the velocity distribution not changing so radically that $w_{||}$ becomes greater than $w_\perp$. This possibility has not been strictly ruled out, although it seems unlikely. Since we have chosen in every case, values that fall at the worst case limit of the error bars, we justifiably argue that the primary results of this paper are determined to at least 70% confidence.

6. Summary

There are four main results (all to 70% confidence or greater) of the work presented here:

- Our analysis shows O^{5+} velocity distribution anisotropy in the streamer legs and stalk and also shows that the microscopic velocity distribution is anisotropic. Evidence for microscopic anisotropy is intriguing because it may be the result of wave-particle interaction processes such as ion cyclotron resonance.

- There is preferential heating of the O^{5+} ions over the protons in the streamer stalk and legs.
- There is no evidence for preferential O^{5+} heating in the core.
- The outflow velocity of the O^{5+} ions is measured above heights of about 4.6 $R_\odot$. We have shown that the outflow speed is between 40 and 75 km s^{-1} at 4.6 $R_\odot$ and between 50 km s^{-1} and 105 km s^{-1} at 5.1 $R_\odot$. At lower heights the outflow speed is below the sensitivity limit of this measurement.

Future work should include empirical modeling of the velocity distributions of a broad range of ions. This should allow determination of upper limits on the contribution of low-frequency transverse wave motions to the empirically determined anisotropy.

The authors would like to thank Larry Gardner, Leonard Strachan, Alexander Panasyuk and Ruth Esser for valuable discussions. This work is supported by NASA under grant NAG5-7822 to the Smithsonian Astrophysical Observatory.

REFERENCES

Allen, L.A., Habbal, S.R., & Hu, Y.Q., J. Geophys. Res., 103, 6551

Banaszkiewicz, M., Axford, W.I., & McKenzie, J.F. 1998, A&A, 337, 940

Brueckner, G.E. et al. 1995, Sol. Phys., 162, 357

Cranmer, S.R., et al. 1999, ApJ, 511, 481

Cranmer, S.R. 2001, J. Geophys. Res., 106, 24937

Feldman, W.C. et al. 1981, J. Geophys. Res., 86, A7, 5408

Fineschi, S., O'Neal, R. & Modigliani, A., unpublished technical report, 1997.

Fineschi, S., Gardner, L.D., Kohl, J.L., Romoli, M., & Noci, G. 1998, SPIE, 3443, 67

Frazin, R.A. et al. 1999, Space Sci. Rev., 87, 189

Frazin, R.A. 2000, ApJ, 530, 1026

Frazin, R.A. 2002, *Empirical Constraints on O^{5+} Outflows and Velocity Distributions in a Solar-Minimum Coronal Streamer*, Ph. D. Thesis, The University of Illinois at Urbana-Champaign

Frazin, R.A. & Janzen, P. 2002, ApJ, 570, 408

Frazin, R.A., Romoli, M., Kohl, J.L, Gardner, L.D., Wang, D., Howard, R.A., & Kucera, T.A. 2002, in *The Radiometric Calibration of SOHO*, ISSI Scientific Report SR-002, eds. A Pauluhn, M.C.E. Huber, & R. von Steiger (Noordwijk: ESA Publications)

Gardner, L.D., et al. 1996, Proc. SPIE, 2831, 2

Gardner, L.D., et al. 2002, in *The Radiometric Calibration of SOHO*, ISSI Scientific Report SR-002, eds. A Pauluhn, M.C.E. Huber, & R. von Steiger (Noordwijk: ESA Publications)

Gosling, J.T., et al. 1981, J. Geophys. Res., 86, 5438

Habbal, S.R., et al. 1997, ApJ, 489, L103

Isenberg, P.A., Lee, M.A., & Hollweg, J.V. 2001, J. Geophys. Res., 106, 5649

Kohl, J.L. *et al.* 1995, Sol. Phys., 162, 313

Kohl, J.L. et al. 1997, Sol. Phys., 175, 613

Laming, J.M. & Feldman, U. 2001, Ap. J., 546, 552

Li, X., Habbal, S.R., Kohl, J.L, & Noci, G. 1998, Ap. J., 501, L133

Mihalas, D. 1978, *Stellar Atmospheres* (Freeman: New York)

Miralles, M. P., Cranmer, S. R., Panasyuk, A. V., Romoli, M., & Kohl, J. L. 2001, ApJ, 549, L257

Miralles, M. P., Cranmer, S. R., & Kohl, J. L. 2001, ApJ, 560, L193 (2001b)

Noci, G., Kohl, J.L., & Withbroe, G.L. 1987, ApJ, 315, 706

Noci, G., & Maccari, L. 1998, A&A, 341, 275

Olsen, E.L., Leer, E., Holzer, T.E. 1994, ApJ, 420, 913

Raymond, J.C. et al. 1997, Sol. Phys., 175, 645

Romoli, M., Frazin, R.A., Kohl, J.L., Gardner, L.D., Cranmer, S.R., Reardon, K., & Fineschi, S. 2002, in *The Radiometric Calibration of SOHO*, ISSI Scientific Report SR-002, eds. A Pauluhn, M.C.E. Humber, & R. von Steiger (Noordwijk: ESA Publications)

Spitzer, L. 1962, *The Physics of Fully Ionized Gases* (New York: Wiley)

Strachan, L., et al. 2000, J. Geophys. Res., 105, 2345

Strachan, L., et al. 2002, ApJ, *in press*

van de Hulst, H.C. 1950, Bull. Astr. Inst. Netherlands, 11, 410, 135

Wang, Y.-M. 1994, ApJ, 437, L67

Wang, Y.-M., et al. 1998, ApJ, 498, L165

Woo, R. 1995, Geophys. Res. Lett., 22, 1393

Wu, S.T., et al. 2000, ApJ, 545, 1101

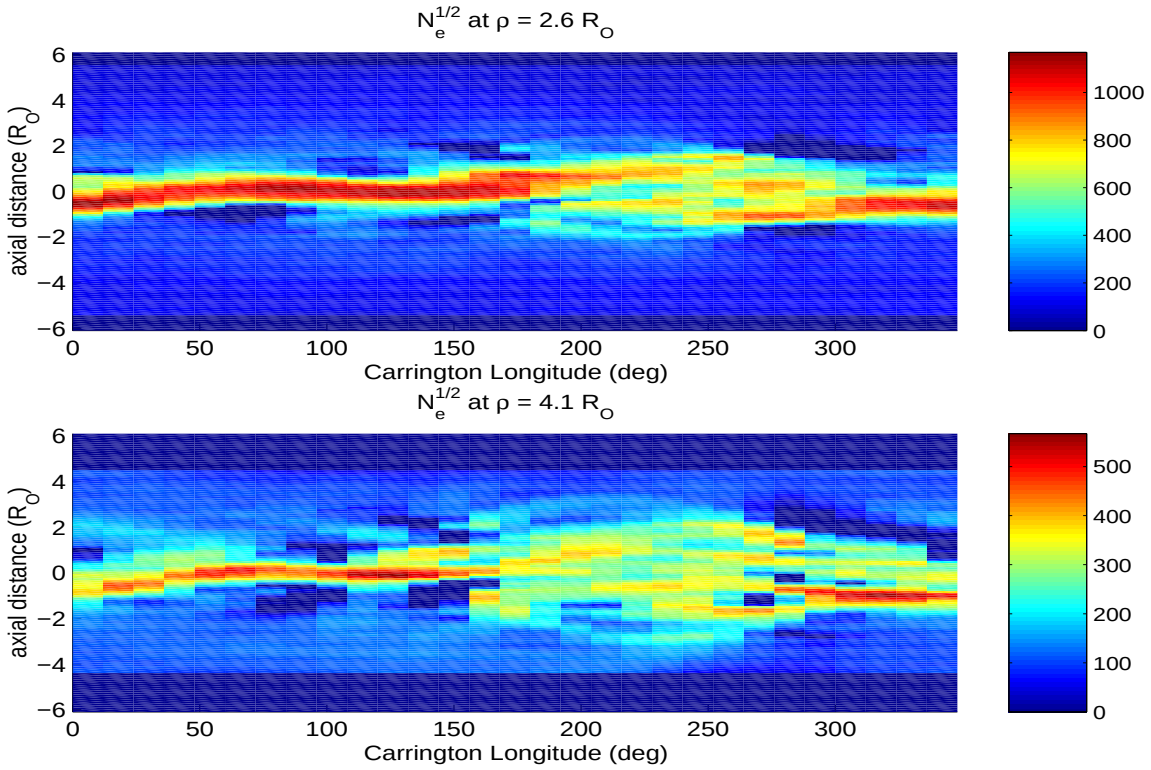

Fig. 8.— Tomographic reconstruction cylindrical shell cuts showing $\sqrt{N_e}$ (in units of $\mathrm{cm}^{-3/2}$) at cylindrical radii of 2.6 and 4.1 $\mathrm{R}_\odot$. The x-axis is the Carrington longitude, and the y-axis is the height above the equatorial plane (in the direction parallel to the axis of the solar pole). The UVCS observations were taken above the west limb, which had a Carrington longitude of about 128° at the time of the observations. This figure shows that the UVCS observations correspond to a part of the coronal structure that was approximately axially symmetric. Both panels exhibit the zero-density artifacts discussed in Frazin & Janzen (2002). The median regularization solution is shown here.

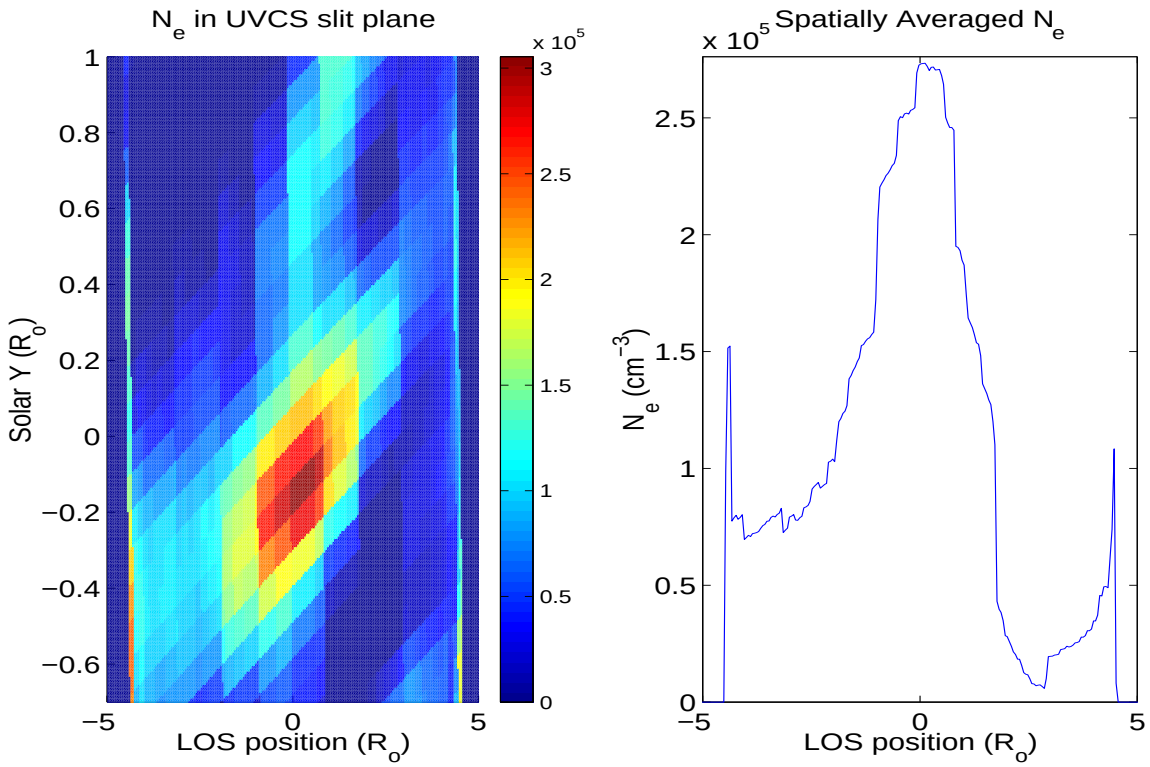

Fig. 9.— Left panel: A tomographic reconstruction of the electron density in the slice of the corona corresponding to the plane of the UVCS slit when it was pointed to 4.1 $R_\odot$. Right: The electron density along the LOS (the x direction). This is the mean density averaged over 0.31 $R_\odot$ along the UVCS slit, centered at solar Y = -0.13 $R_\odot$ (south of the equatorial plane). The spikes at the edges of the figure are effects due to the finite size of the computation volume. Several *zero density artifacts* (see Frazin & Janzen 2002) can be seen in the left panel, but they do not touch the region studied in this paper.

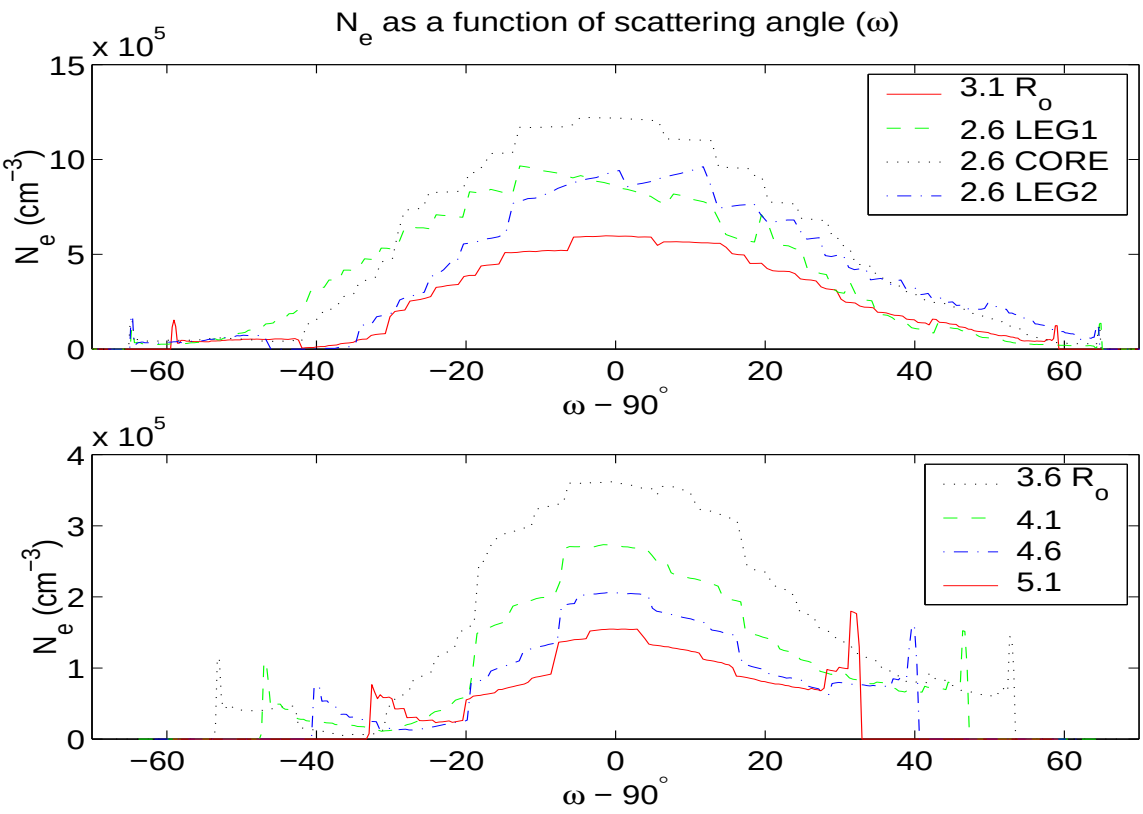

Fig. 10.— The electron density as a function of the scattering angle ω for the UV spectral observations reported here. These plots were determined from the tomographic reconstruction as in Figure 9. Edge artifacts are more apparent at the larger heights because the line of sight cuts a smaller chord through the computation volume.

observation	$<\mid \omega - 90^\circ \mid>$
2.6 $R_\odot$, LEG1	22
2.6 $R_\odot$, CORE	22
2.6 $R_\odot$, LEG2	24
3.1 $R_\odot$	21
3.6 $R_\odot$	20
4.1 $R_\odot$	18
4.6 $R_\odot$	16
5.1 $R_\odot$	15

Table 2: The mean of ($\mid \omega - 90^\circ \mid$) as defined in equation (3) and determined from the tomographic reconstruction. The values above 3.1 $R_\odot$ are underestimates due to the finite volume of the tomographic computation cylinder.

height ($R_\odot$)	anisotropy constraint $w_\parallel/w_\perp$	velocity constraint $u_\parallel$ (km/s)
2.6 (LEG1)	< 0.5	< 10
2.6 (CORE)	≤ 1.0	< 15
2.6 (LEG2)	< 0.25	< 5
3.1	< 0.6	< 30
3.6	< 0.7	< 40
4.1	< 0.6	< 35
4.6	< 1.6[a]	$40 < u_\parallel < 75$[b]
5.1	< 4.0[a]	$50 < u_\parallel < 105$[b]

Table 3: O^{5+} velocity distribution constraints. The most probable speed in the perpendicular direction $w_\perp$ is given by the measured line widths in Figure 6, although see the text for details.

[a] These values are discussed in section 5.

[b] This requires $w_\parallel/w_\perp \leq 0.6$ (see section 5)

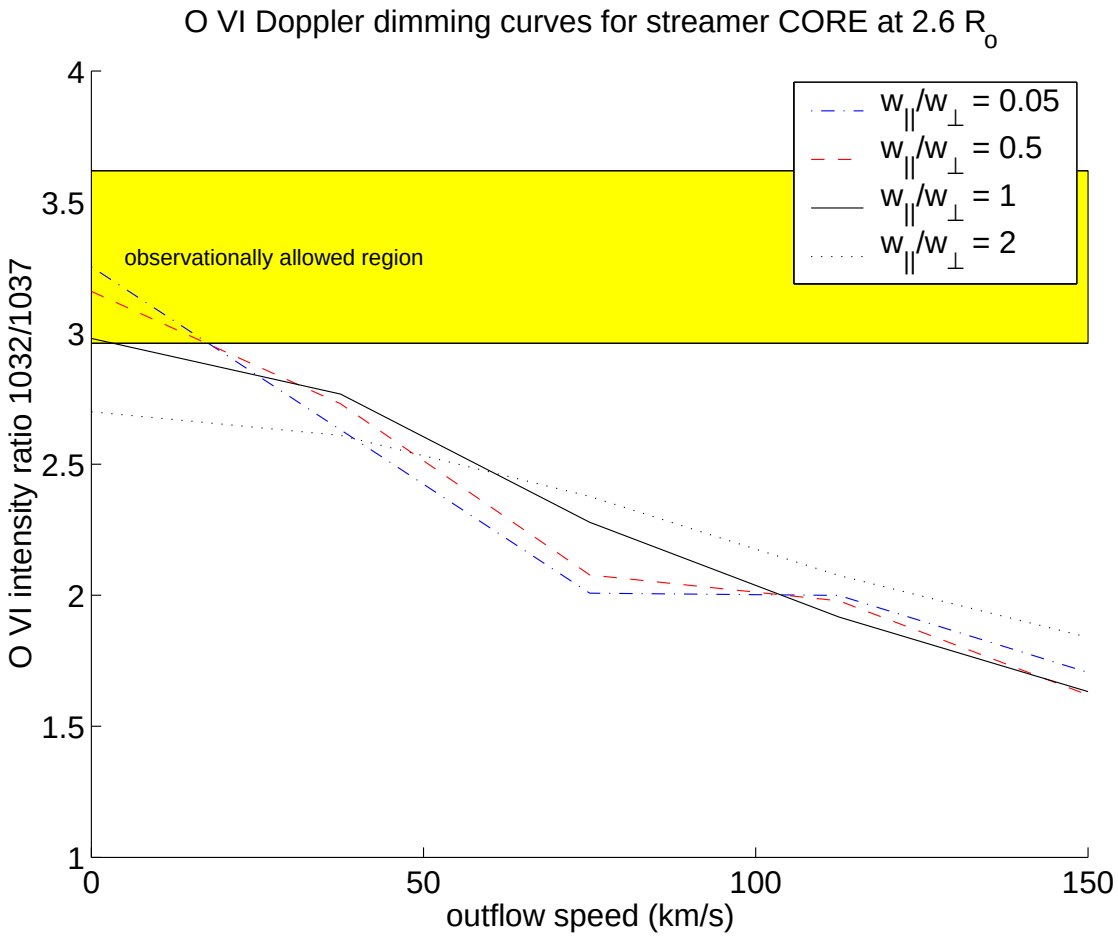

Fig. 11.— O^{5+} Doppler dimming curves for the streamer CORE at 2.6 $R_\odot$ (see Figure 2). The location of the observationally allowed region (shaded band) is given by the value of the measured intensity ratio of the O VI λ1032, 1037 Å doublet, and its width is determined by the $\pm 1\sigma$ uncertainty of the measurement. The curves show the predicted O VI doublet intensity ratio as a function of outflow speed and are determined via the spectral synthesis procedure. Each curve corresponds to one value of the anisotropy ratio $w_{||}/w_\perp$, where $w_{||}$ and $w_\perp$ are the most probable speeds in the directions parallel and perpendicular to the magnetic field, respectively. This figure shows $w_{||}/w_\perp \leq 1.0$.

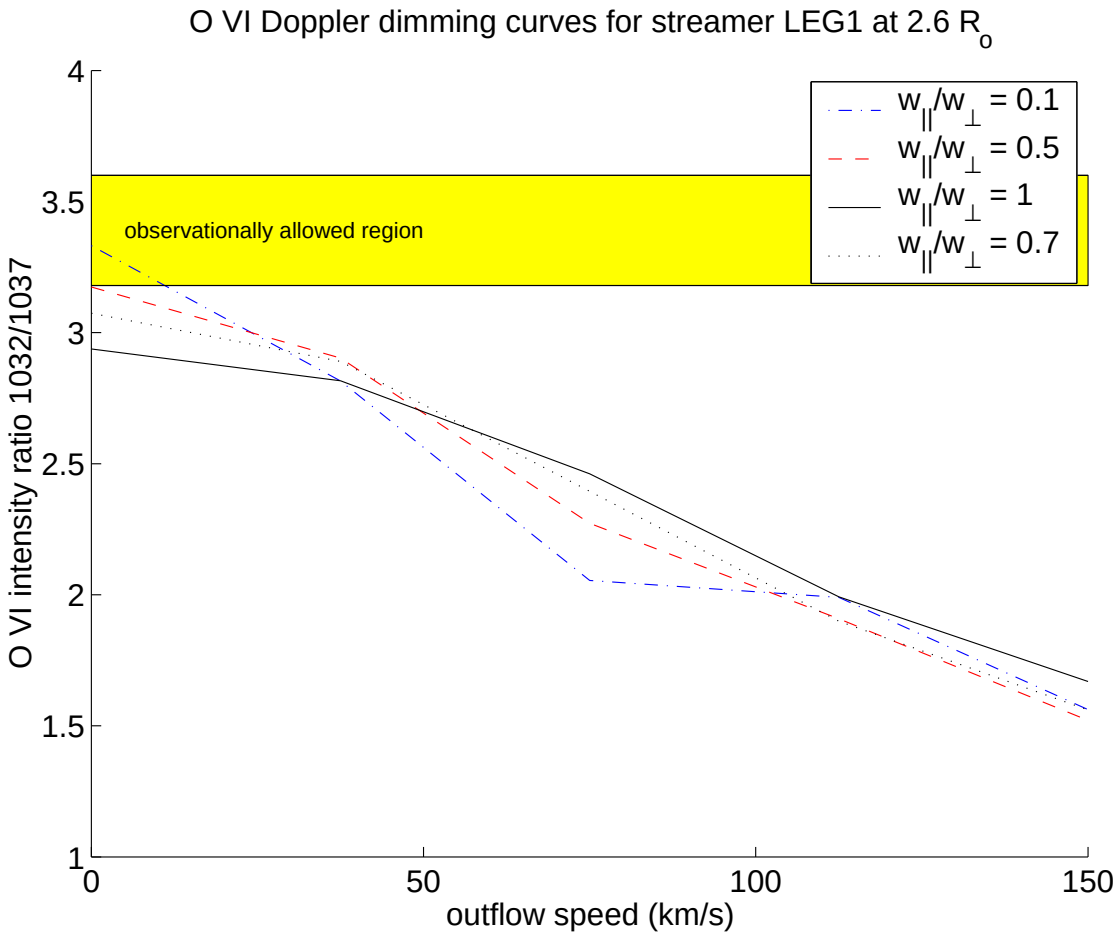

Fig. 12.— O^{5+} Doppler dimming curves for the streamer LEG1 region at 2.6 $R_\odot$ (see Figure 2). This figure shows that the O^{5+} velocity distribution is anisotropic, with $w_{||}/w_\perp < 0.5$. Note that the curve corresponding to the isotropic velocity distribution (solid) does not come close to the observationally allowed region.

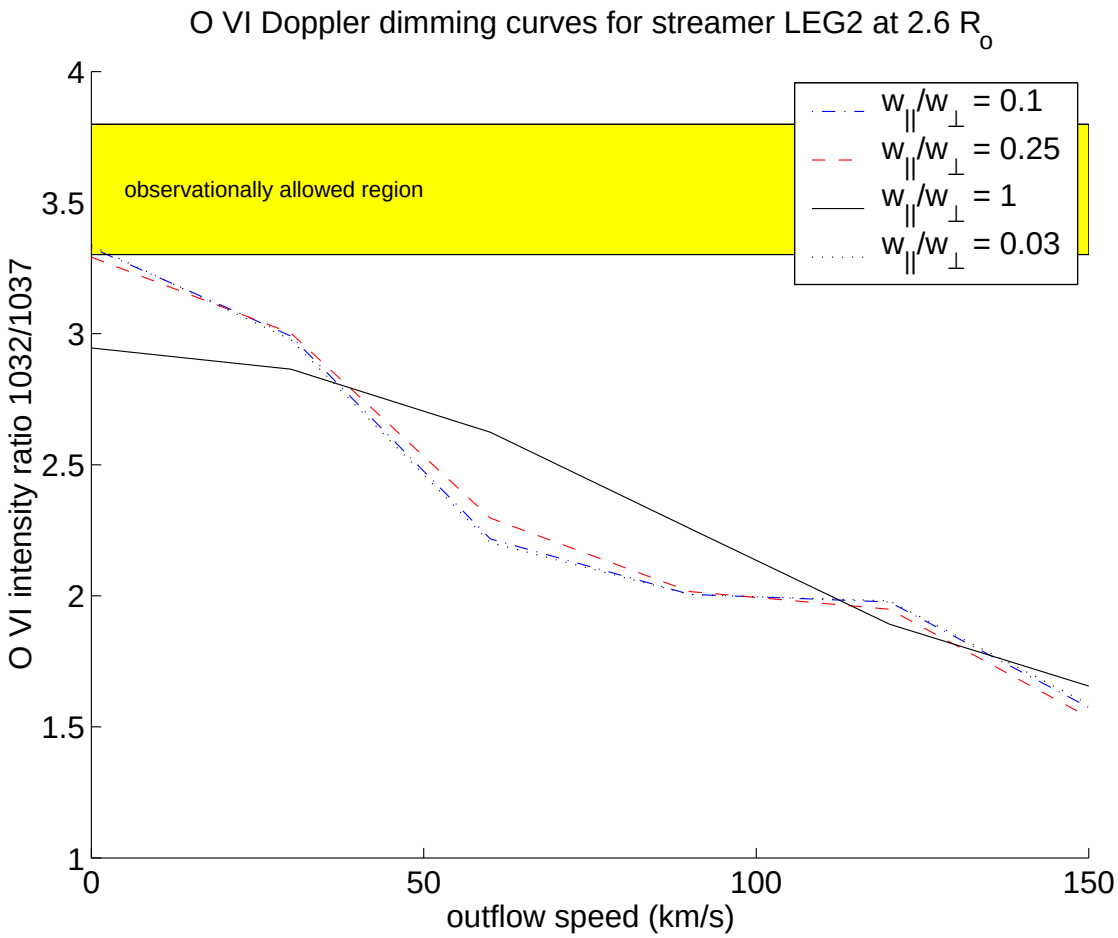

Fig. 13.— O^{5+} Doppler dimming curves for the streamer LEG2 region at 2.6 $R_\odot$ (see Figure 2). The curves for $w_{||}/w_\perp = 0.1$ and 0.03 are nearly coincident. This figure shows that the O^{5+} velocity distribution is anisotropic, with $w_{||}/w_\perp < 0.25$. Note that the curve corresponding to the isotropic velocity distribution (solid) does not come close to the observationally allowed region.

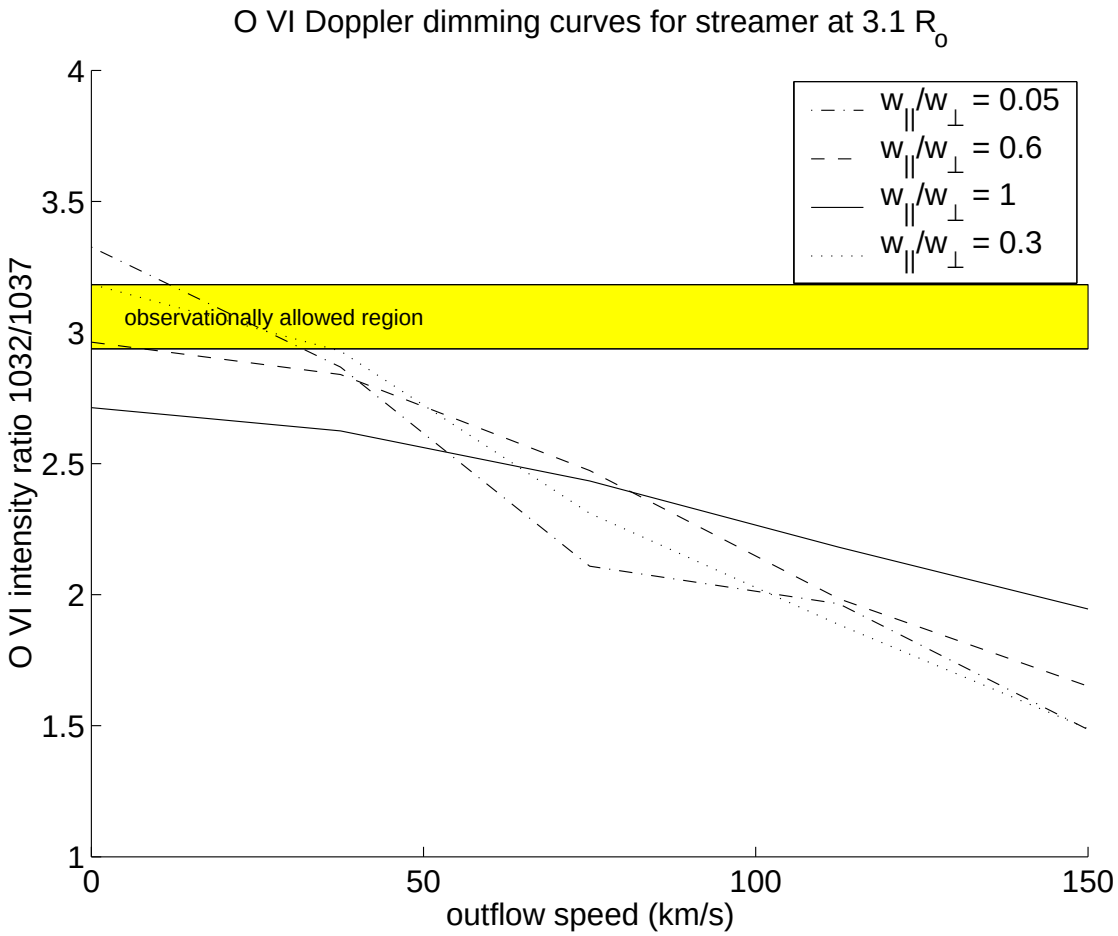

Fig. 14.— O^{5+} Doppler dimming curves for the streamer at 3.1 $R_\odot$. This figure shows that the O^{5+} velocity distribution is anisotropic, with $w_{||}/w_\perp < 0.6$. Note that the curve corresponding to the isotropic velocity distribution (solid) does not come close to the observationally allowed region.

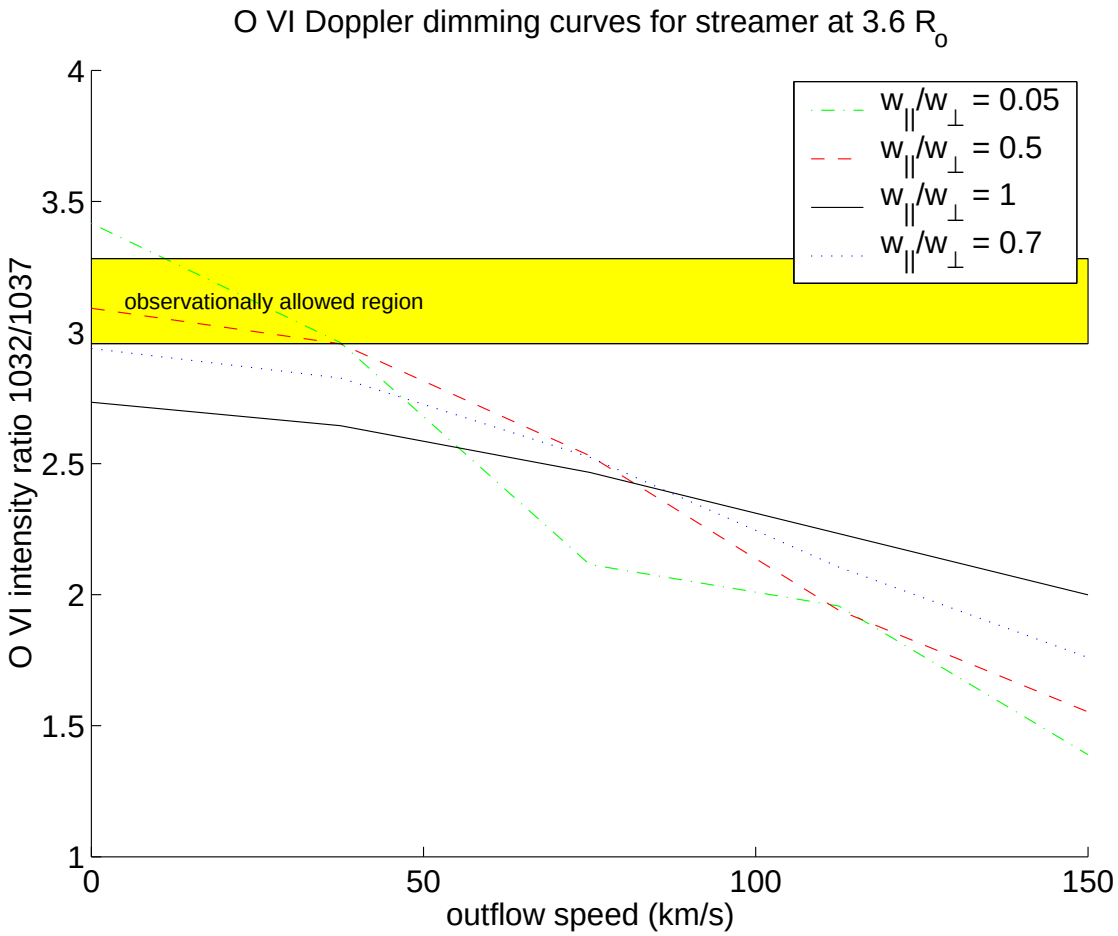

Fig. 15.— O^{5+} Doppler dimming curves for the streamer at 3.6 $R_\odot$. This figure shows that the O^{5+} velocity distribution is anisotropic, with $w_{||}/w_\perp < 0.7$. Note that the curve corresponding to the isotropic velocity distribution (solid) does not come close to the observationally allowed region.

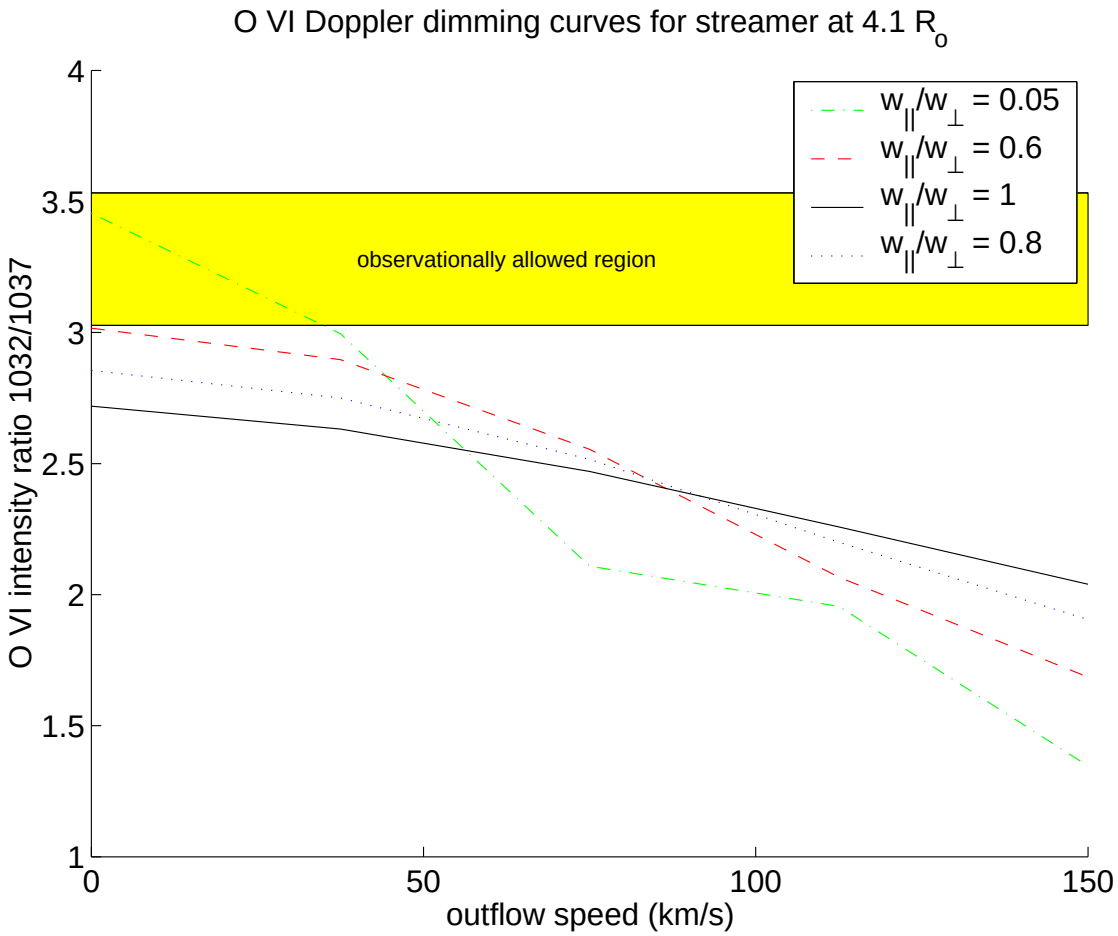

Fig. 16.— O^{5+} Doppler dimming curves for the streamer at 4.1 $R_\odot$. This figure shows that the O^{5+} velocity distribution is anisotropic, with $w_{||}/w_\perp < 0.6$. Note that the curve corresponding to the isotropic velocity distribution (solid) does not come close to the observationally allowed region.

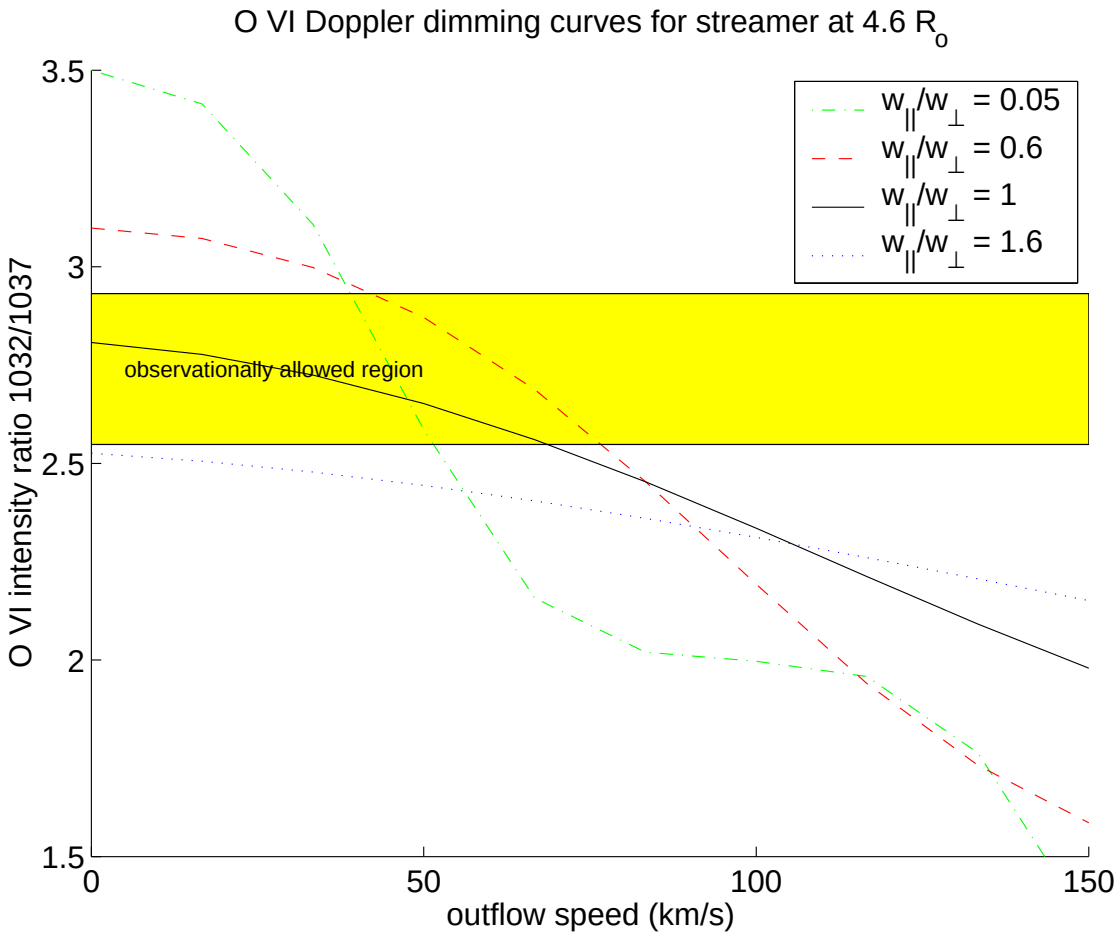

Fig. 17.— O^{5+} Doppler dimming curves for the streamer at 4.6 $R_\odot$. If $w_{||}/w_\perp < 0.6$ (see text), then this figure shows 40 km $s^{-1} < u < 70$ km s^{-1}.

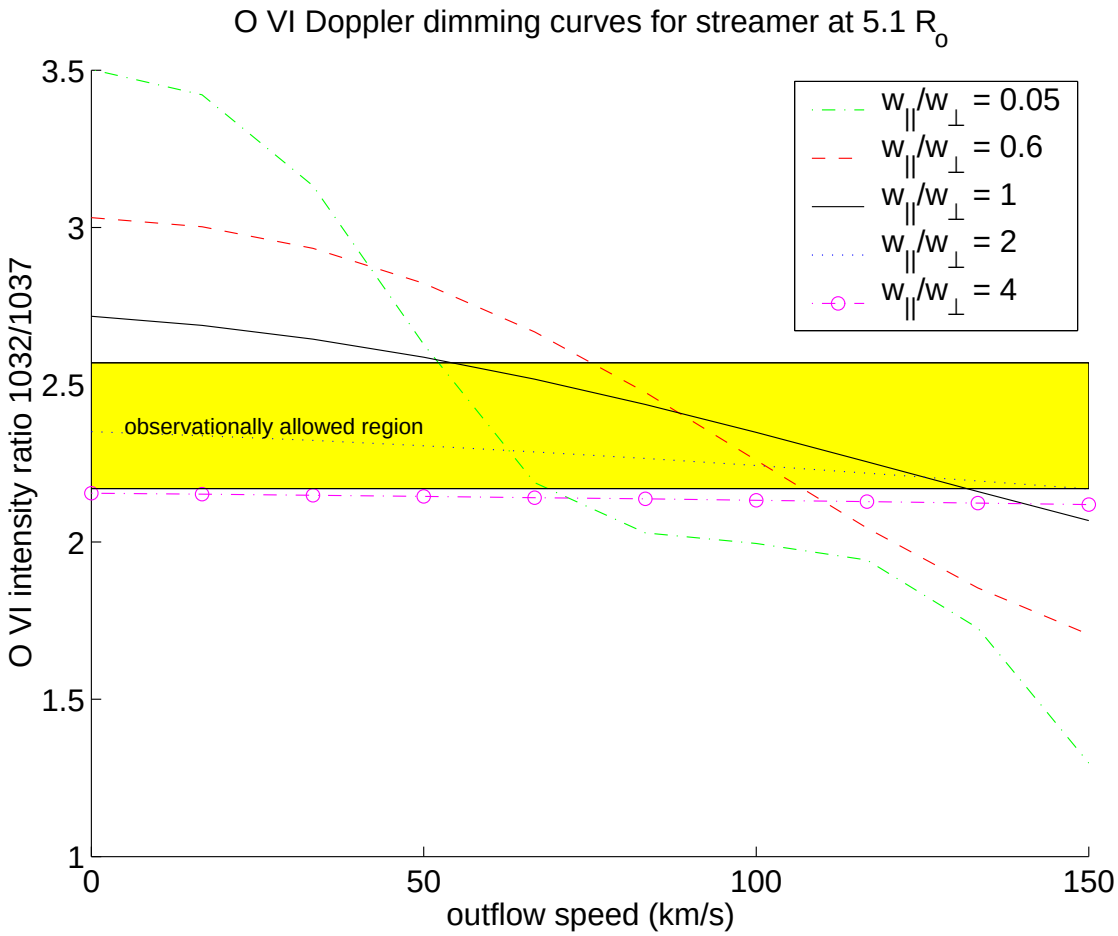

Fig. 18.— O^{5+} Doppler dimming curves for the streamer at 5.1 $R_\odot$. If $w_{||}/w_\perp < 0.6$ (see text), then this figure shows 50 km $s^{-1} < u < 105$ km s^{-1}.